Mechanisms shaping wind convergence under extreme synoptic situations over the Gulf Stream region

Victor Rousseau, Emilia Sanchez-Gomez, Rym Msadek, Marie-Pierre Moine

Mechanisms Shaping Wind Convergence under Extreme Synoptic Situations over the Gulf Stream Region

VICTOR ROUSSEAU,[a] EMILIA SANCHEZ-GOMEZ,[a] RYM MSADEK,[a] AND MARIE-PIERRE MOINE[a]

[a] *CECI, Université de Toulouse, CNRS, CERFACS, Toulouse, France*

(Manuscript received 16 September 2020, in final form 15 July 2021)

ABSTRACT: Air–sea interaction processes over the Gulf Stream have received particular attention over the last decade. It has been shown that sea surface temperature (SST) gradients over the Gulf Stream can alter the near-surface wind divergence through changes in the marine atmospheric boundary layer (MABL). Two mechanisms have been proposed to explain the response: the vertical mixing mechanism (VMM) and the pressure adjustment mechanism (PAM). However, their respective contribution is still under debate. It has been argued that the synoptic perturbations over the Gulf Stream can provide more insight into the MABL response to SST fronts. We analyze the VMM and PAM under different atmospheric conditions obtained from a classification method that is based on the deciles of the statistical distribution of winter turbulent heat fluxes over the Gulf Stream. The lowest deciles are associated with weak air–sea interactions and anticyclonic atmospheric circulation over the Gulf Stream, whereas the highest deciles are related to strong air–sea interactions and a cyclonic circulation. Our analysis includes the low- and high-resolution versions of the ARPEGEv6 atmospheric model forced by observed SST, and the recently released ERA5 global reanalysis. We find that the occurrence of anticyclonic and cyclonic perturbations associated with different anomalous wind regimes can locally modulate the activation of the VMM and the PAM. In particular, the PAM is predominant in anticyclonic conditions, whereas both mechanisms are equally present in most of the cyclonic conditions. Our results highlight the role of the atmospheric circulation and associated anomalous winds in the location, strength, and occurrence of both mechanisms.

KEYWORDS: Atmosphere–ocean interaction; Extreme events; Marine boundary layer; Synoptic-scale processes; Small-scale processes; Surface fluxes

1. Introduction

The Gulf Stream (GS), one of the major western boundary currents, flows poleward along the western flank of the North Atlantic Ocean basin, bringing warm and salty waters from the tropics to higher latitudes. At midlatitudes, the Gulf Stream encounters the cold Labrador Current coming from the western branch of the subpolar gyre, which generates sharp sea surface temperature (SST) gradients or fronts. The ocean in the GS region is characterized by the presence of meanders that can separate from the main current to create smaller structures called mesoscale eddies. Recently, a lot of attention has been given to SST fronts and the associated oceanic mesoscale structures in shaping air–sea interactions in the region. The development and use of higher-resolution observations and climate models have revealed that midlatitude SST fronts can influence the overlying atmospheric circulation, a feature whose study was limited in coarse-resolution observations and in standard-resolution climate models. Minobe et al. (2008) and Kuwano-Yoshida et al. (2010) showed that mesoscale SST structures are collocated with a convective precipitation band due to low-level wind convergence and enhanced evaporation over the warm part of the SST front. Hence, they suggested that near-surface wind convergence anomalies can affect the free troposphere locally through vertical motion and convective precipitation. Two main mechanisms occurring in the marine atmospheric boundary layer (MABL) have been proposed to explain the influence of SST fronts and mesoscale oceanic eddies on the near-surface wind divergence and convergence (Chelton et al. 2004; Minobe et al. 2008; Small et al. 2008; O'Neill et al. 2010; Putrasahan et al. 2013; Chelton and Xie 2010; Ma et al. 2016; Roberts et al. 2016). One mechanism is the so-called vertical mixing mechanism (VMM), which has been described both, in observational and modeling studies (Chelton and Xie 2010; Putrasahan et al. 2013; Takatama et al. 2015; Hayes et al. 1989; Chelton et al. 2001; O'Neill et al. 2003; Roberts et al. 2016; Piazza et al. 2016; Xie et al. 2002). The VMM consists of an intensification of near-surface winds over a warm ocean. Indeed, the warm part of the SST front destabilizes the overlying atmosphere, which can strengthen the momentum transfer and the vertical mixing in the MABL. The momentum from aloft is then transported downward, thus accelerating the near-surface winds (Sweet et al. 1981; Wallace et al. 1989; Hayes et al. 1989). These spatial variations in wind stress magnitude result in wind stress divergence when the wind blows perpendicular to the SST front, and to a wind stress curl when the wind blows parallel to the front (Spall 2007; O'Neill et al. 2017; Chelton et al. 2004). The VMM influence on the MABL can hence be estimated by the linear relationship between the downwind component of the SST gradient (DW_SST) and the near-surface wind divergence, or by the relationship between the crosswind component of the SST gradient and the near-surface wind curl.

Another mechanism that can explain the influence of oceanic SST fronts on the atmosphere is the so-called pressure

Denotes content that is immediately available upon publication as open access.

Corresponding author: Victor Rousseau, vmr.rousseau@gmail.com

DOI: 10.1175/JCLI-D-20-0719.1

adjustment mechanism (PAM), which was originally introduced by Lindzen and Nigam (1987). It can be explained by the different heating of the atmosphere on each side of the SST front, which creates low pressure over warm waters and high pressure over cold waters. This pressure gradient induces a secondary atmospheric circulation with winds blowing from cold to warm SSTs, creating near-surface convergence or divergence above the warm part or cold part, respectively, of the SST front. The PAM can be characterized by the linear regression between the Laplacian of sea level pressure [LAP(SLP)] and the near-surface wind divergence over the GS (Minobe et al. 2008). Several observational and modeling studies have shown that over the GS, a positive LAP(SLP) is located over the wind convergence zone, and conversely a negative LAP(SLP) is collocated with positive divergence wind anomalies, which suggests that the PAM may play an important role in the MABL response to the SST front (Takatama et al. 2015; Bryan et al. 2010; Putrasahan et al. 2013).

Up to now, the relative contribution of the PAM and VMM in shaping the MABL response to the GS SST front is still unclear (Takatama et al. 2015; O'Neill et al. 2017; Masunaga et al. 2020a,b). It has been suggested that the importance of the PAM and VMM depends on the background wind conditions (Spall 2007; Small et al. 2008; Chelton and Xie 2010), the geographical location of the SST front (Chelton and Xie 2010), and the season of the year (Minobe et al. 2010; Putrasahan et al. 2013). Moreover, most of the studies that characterized the role of the PAM and VMM focused on time-mean fields (i.e., on fields averaged over a given time period). Until now, the PAM has been put forward to explain the majority of the time mean of wind convergence in opposition to the VMM (Minobe et al. 2008; Takatama et al. 2015). However, the presence of strong LAP(SLP) values over the GS is not only due to mesoscale SST modulations. Brachet et al. (2012) further argued that, besides the thermal SST forcing, migratory synoptic-scale cyclones can exert an important signature on the LAP(SLP). Therefore, at synoptic scale, the LAP(SLP) signal could be decomposed into the pure PAM process, the SLP response to mesoscale SST, and a dynamical component linked to synoptic activity.

Moreover, recently, O'Neill et al. (2017) suggested that synoptic-scale processes, like extratropical cyclones, can play a dominant role in controlling the time-mean near-surface wind divergence and convergence over the GS. They further argued that time-mean averages could mask some important features that could be key in understanding the MABL response to SST fronts. Indeed, synoptic-scale atmospheric disturbances are associated with an anomalously large turbulent heat flux release from the ocean and an intense baroclinicity in the lower layers of the atmosphere. Hence, the response of the MABL to SST fronts might also be influenced by air–sea turbulent fluxes and surface wind variations at synoptic scales (Parfitt 2014). Further, it has been shown that extratropical cyclones can contribute significantly to the near-surface convergence (Vannière et al. 2017). In addition to that, several studies have shown that the time-mean pattern of surface convergence near the Gulf Stream could result mainly from the local strengthening of atmospheric fronts (Parfitt et al. 2016; Parfitt and Seo 2018), which also highlights the importance of the synoptic-scale processes on the GS convergence zone.

Based on atmospheric reanalysis, recent studies have shown that exploring MABL processes at daily time scale, by isolating extreme events or by selecting specific case studies, can provide more insights about the mechanisms responsible of shaping air–sea interactions in the GS region rather than studying a classical time-mean analysis (O'Neill et al. 2017; Masunaga et al. 2020a,b). The main goal of this study is to investigate the role of the PAM and VMM in shaping the surface wind divergence over the GS. Most of the studies cited above have used only atmospheric reanalysis or one realization of an atmospheric stand-alone simulation. As internal climate variability is important over midlatitude regions, the use of a large sample size could be beneficial to robustly identify the influence of SST fronts on the overlying atmosphere within the context of extreme air–sea interactions. Here, in addition to the analysis of state-of-the-art atmospheric reanalysis, two ensembles of 10 members of atmosphere-only model simulations forced by observed SST and performed at two different horizontal resolutions, 140 and 50 km, are used. These experiments were done within the framework of the H2020 PRIMAVERA project through the HighResMIP initiative (Haarsma et al. 2016). Our analysis is based on a classification of different synoptic situations defined from the turbulent heat flux distribution over the GS, following Parfitt and Czaja (2016). We distinguish atmospheric patterns corresponding to weak and strong turbulent heat flux release from the ocean to the atmosphere during winter.

In section 2 we present the reanalysis and model experiments used in this study. The classification method of different synoptic situations, based on the distribution of turbulent heat flux, is described in section 3. Section 4 describes the PAM and VMM mechanisms and their role in the simulated near-surface wind convergence/divergence for the different synoptic patterns. A summary and discussion are given in section 5.

2. Data and methods

a. Numerical experiments and reference datasets

This study uses both a high-resolution (HR) and a low-resolution (LR) version of the ARPEGE-Climat model (Roehrig et al. 2020), which is the atmospheric component of the CNRM-CM6-1 coupled model, developed by the Centre National de Recherches Météorologiques/Centre Européen de Recherche et de Formation Avancée en Calcul Scientifique (CNRM/CERFACS) group (Voldoire et al. 2019). The HR model operates with a T359 truncation, which corresponds to ~50-km horizontal resolution at midlatitudes. The LR grid has a T127 truncation, which is equivalent to 140-km horizontal resolution at midlatitudes. Both models share the same vertical discretization with 91 vertical levels. We analyze the atmospheric-only simulations performed within the HighResMIP of phase 6 of the Coupled Model Intercomparison Project (CMIP6) (Eyring et al. 2016; Haarsma et al. 2016). Because the HighResMIP initiative seeks to investigate the role of model resolution on the representation of European climate, the LR

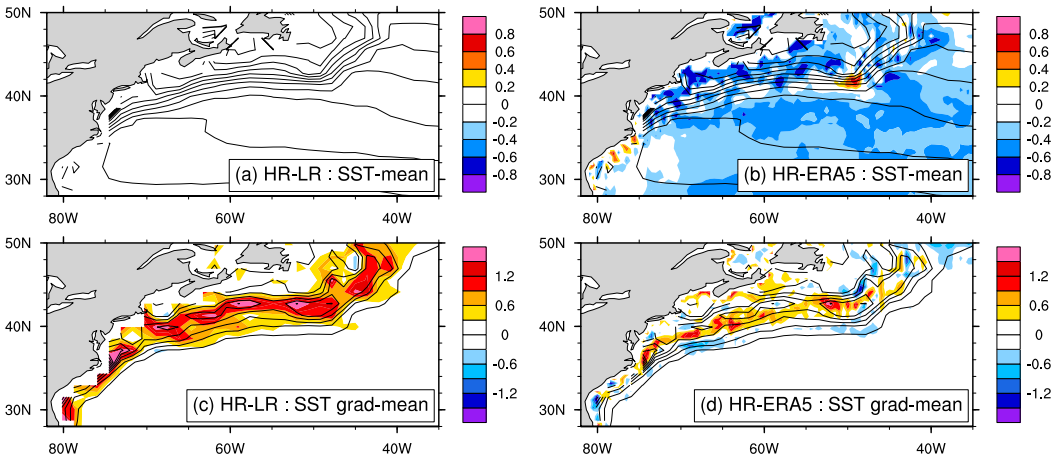

FIG. 1. Differences between SST mean patterns for (a) HR − LR and (b) HR − ERA5. The shading corresponds to the SST differences (°C), and the contours correspond to the SST values for HR (every 2°C); differences between SST gradient mean patterns for (c) HR − LR and (d) HR − ERA5. The shading corresponds to the SST gradient differences [°C (100 km)$^{-1}$], and the contours correspond to SST gradient values for HR [every 1°C (100 km)$^{-1}$].

and HR configurations use the same model parameters and differ only by their horizontal resolution, except for a few parameterizations that are scale-dependent and could not be kept exactly the same. In the atmosphere-only experiments, the SST and sea ice concentration are imposed at the boundaries and extracted from the ¼° HadISST reanalysis dataset (Kennedy et al. 2017). This dataset has been developed within the PRIMAVERA project (Haarsma et al. 2016) and has been also used in Rowell (2019), Thomas et al. (2019), and Roberts et al. (2020). To be used as boundary condition for the ARPEGE model, the HadISST SST dataset is interpolated on the HR and LR grids respectively. Each simulation is then run over the period 1950–2014, producing so-called AMIP experiments. For each model configuration, 10 members have been produced, by slightly perturbing the atmospheric initial conditions. It is noteworthy that this study provides a large time sample to study air–sea interactions in the MABL.

Both ensembles of simulations are compared with the recently developed high-resolution reanalysis ERA5 (Hersbach et al. 2020; Hersbach 2018) as well as with the lower-resolution ERA-Interim (ERAI herein) reanalysis (Simmons et al. 2007; Berrisford et al. 2009). ERA5 operates on a TL639 grid that corresponds to a horizontal resolution of approximately 30 km with 137 sigma–pressure hybrid vertical levels. ERAI was created on a T255 grid, which results in a nominal resolution of 80 km, with 60 pressure levels. Both reanalyses are available from 1979 to 2018. We focus on the winter season, defined as the December– February mean (DJF), of daily fields, since the turbulent heat flux release from the ocean to the atmosphere over the GS region is strongest during these months.

First, the mean SSTs and the gradient of SST is examined for HR, LR, and ERA5. Figure 1 represents differences in SST and SST gradient for HR-LR and HR-ERA5. Note that HR is interpolated onto the LR grid and ERA5 onto the HR grid to perform the comparison. As expected, HR and LR SSTs are identical (Fig. 1a). In terms of SST gradient, HR reveals a more intense gradient than LR over the SST front location, which is consistent with smaller grid spacing in the HR model (Fig. 1c). The SST gradient is 20% more intense in HR than in LR. Figure 1b shows that HR-SSTs are generally colder than ERA5 SSTs in most part of the GS domain, with differences that can reach more than 0.5°C near the cold part of the SST front. In terms of SST gradient, HadISST reanalysis presents a more intense gradient (10%) than ERA5 SST (Fig. 1d).

b. *Method for wintertime classification of synoptic situations*

We use a clustering method to identify synoptic situations according to different magnitudes of turbulent heat flux release from the ocean to the atmosphere. This method was first introduced by Parfitt and Czaja (2016). Figure 2 shows the wintertime mean turbulent heat flux released to the atmosphere (THF) for both model configurations and in the reanalyses. The THF is defined by the latent plus sensible heat flux, with positive values upward. The THF magnitude and structure are very similar in the HR and LR configurations, with values reaching up to 550 W m^{-2}. The simulated values are larger than in ERA5 and ERAI, with a model mean bias of +15% in HR and +12% in LR with respect to ERA5. This overestimation of the THF over the ocean is a known bias of the ARPEGE atmospheric model both in forced and coupled mode (Roehrig et al. 2020). Note that although the model climatology shown in Fig. 2 results from the average of 10 members, considering each member separately gives a comparable result.

The clustering approach is based on the distribution of daily values of THF computed over a selected box (31.5°–39°N, 58.5°–75°W; see Fig. 2), which captures the maximum of the wintertime turbulent heat flux exchange over the GS. Other boxes have been used to check the robustness of the method and the results described below are unchanged.

Following Parfitt and Czaja (2016), an air–sea interaction index (ASII) is defined as

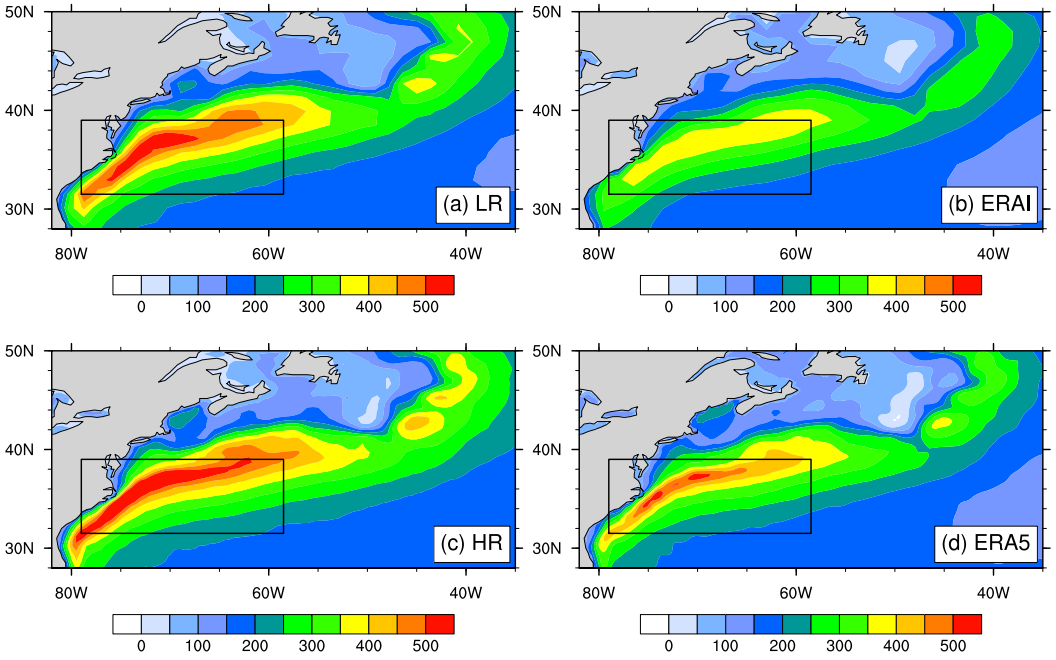

FIG. 2. Time mean (DJF) for the turbulent heat flux ($W\,m^{-2}$) for (a) LR, (b) ERA-I, (c) HR, and (d) ERA5.

$$\mathrm{ASII}(t) = \int_{\mathrm{domain}} \mathrm{THF}(x, y, t)\, dx\, dy, \tag{1}$$

where x is longitude, y is latitude, and t is time. The ASII values can be reordered from low to high values to build a probability distribution function (PDF). The latter is used to determine the deciles of the distribution. Low deciles are associated with weak THF release or weak air–sea interaction, whereas higher deciles are associated with strong air–sea exchanges. We define 10 clusters, which correspond to the 10 deciles of the PDF. Composites are then defined by averaging, for various variables of interest (e.g., sea level pressure anomalies, surface wind divergence), the days belonging to the same decile. The corresponding patterns are used to characterize the atmospheric situation for weak and strong air–sea interactions. To characterize near-surface wind and divergence composites, we use the 10-m wind field since the latter is directly related to the turbulent heat fluxes. Previous studies that characterize the MABL response to SST fronts use indifferently the 10-m winds and wind stress. The conclusions about the importance of the MABL mechanisms are in general unaffected.

We can further estimate the contribution of each decile to the time mean. For instance, the contribution of the last decile to the mean for a given field X is given by

$$\frac{1}{N} \sum_{\mathrm{ASII}=90\%}^{100\%} X(\mathrm{ASII}), \tag{2}$$

where N is the total number of wintertime days.

Note that the ASII and the composite maps are calculated separately for each dataset and no interpolation is performed at this stage. Differences between the models and ERA5 reanalysis are computed after interpolating the fields onto the LR grid. To maximize the ensemble size, the THF distribution, the ASII, and the decile computations are performed by considering the full distribution of the 10 members for LR and HR separately. For the composite analysis, composite maps are obtained for each member, and maps of the ensemble mean are computed from them. We assess the statistical significance of the differences using a bootstrapping method. All of the statistics shown in the following were computed using a large number (1000) of bootstrap data samples. In addition, because SST satellite observations are usually unavailable during the period from the 1950s to the 1970s, the sensitivity of the results to the time period considered for SSTs was investigated by repeating the clustering analysis over the more recent 2000–14 period. The THF values and decile patterns were almost unaffected.

3. Role of extreme THF conditions in shaping surface wind divergence over the GS

a. Simulated and observed distribution of the THF over the GS

We first analyze the distribution of several indices that characterize air–sea interactions by comparing the simulated distributions in the LR and HR models with those in ERA5 and ERAI (Fig. 3a). All of the distributions are computed using daily-mean data. The thick line represents the PDF calculated from the full distribution of the 10 members for each simulation. The shading indicates the spread obtained for the individual members for HR and LR. This provides an estimate of internal climate variability and gives an idea of the importance of considering several members to study differences between models and reanalyses. HR and LR overestimate the

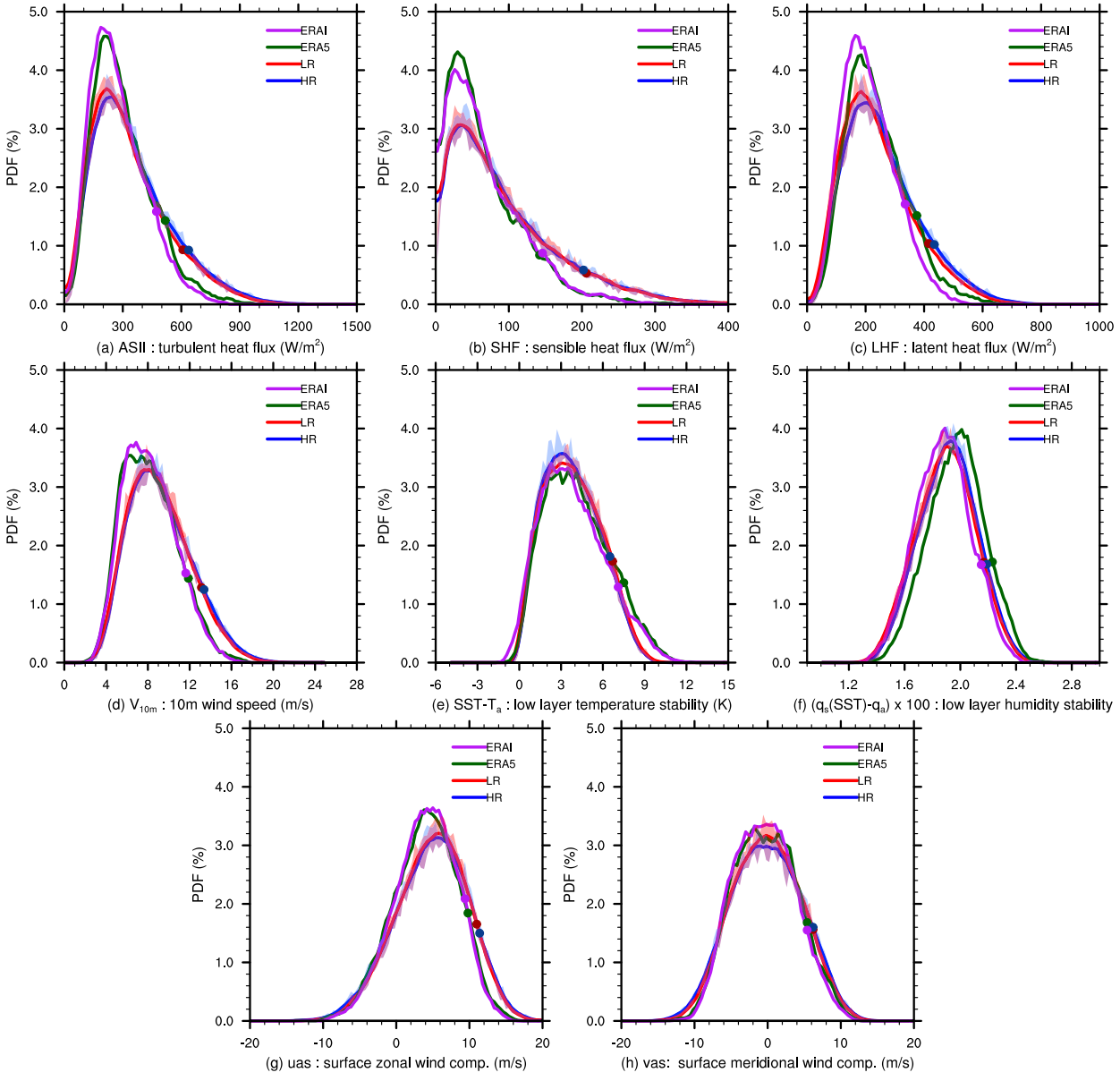

FIG. 3. Probability density function of the daily values for the (a) ASII (air–sea interaction index), (b) sensible heat flux, (c) latent heat flux, (d) 10-m wind speed, (e) near-surface temperature stability, (f) near-surface humidity stability, (g) 10-m zonal wind component, and (h) 10-m meridional wind component. Values are shown for HR (blue), LR (red), ERA-I (purple), and ERA5 (green). The daily data used to build the PDFs are obtained from the spatial average over the box outlined in Fig. 1.

THF values relative to ERA5 and ERAI for bins above 500 W m^{-2}. The PDFs also suggest that the variability in the models, measured as the standard deviation, is larger than in ERA5. We have computed the standard deviation for THF, and it results to be 218, 213, and 173 W m^{-2} respectively for HR, LR, and ERA5. This represents a bias of +26% and +23% respectively for HR and LR in comparison with ERA5. For extreme values of THF, HR and LR are around 20% larger than ERA5. However, for THF values closer to or smaller than the mean (below 500 W m^{-2}), ERA5 displays values that are 15% larger than the simulated ones.

HR and LR differences indicate that THF is about 5% greater in HR only for the highest deciles. This difference is however not statistically significant since it lies within the intermember spread, which suggests a limited role of increased model resolution in this model.

To further understand what controls the distribution of THF in the models and in reanalysis, the THF is decomposed into its latent (LHF) and sensible (SHF) heat flux contributions (Figs. 3b,c). The PDFs of the simulated latent and sensible heat fluxes indicate that the largest values of both contributions are overestimated relative to the reanalysis, whereas the weaker

fluxes are underestimated in both models. The impact of model resolution, though small, is more important for the LHF for values close to the mean.

Our results suggest that increasing the horizontal resolution of the atmospheric model from 140 to 50 km yields only small changes in the simulated THF for the ARPEGE model.

To further examine the LHF and SHF differences found in Fig. 3 we use the bulk formulation:

$$\mathrm{LHF} = \mathrm{LHF}[V_{10\mathrm{m}}, q_s(\mathrm{SST}) - q_a] \quad \text{and} \tag{3}$$

$$\mathrm{SHF} = \mathrm{SHF}(V_{10\mathrm{m}}, \mathrm{SST} - T_a), \tag{4}$$

which indicates that the latent heat flux is a function of the 10-m wind speed $V_{10\mathrm{m}}$ and the near-surface humidity stability $q_s(\mathrm{SST}) - q_a$. The sensible heat flux depends on the 10-m wind speed and the near-surface temperature stability $\mathrm{SST} - T_a$, where T_a is the air temperature at 2 m.

Figure 3d shows that the extreme surface winds in the models are stronger than in the reanalyses whereas the indices defining the near-surface temperature and humidity stability show weaker than observed values for the rightmost part of the distribution, in particular in comparison with ERA5 (Figs. 3e,f). We can further conclude that the overestimation of the 10-m wind speed in the models is due to the extreme positive values of the zonal component (Figs. 3g,h). This is consistent with a well-known zonal bias of the ARPEGE model (Roehrig et al. 2020). In summary, HR and LR overestimate the extreme high values of the wind speed over the GS. The effect of stronger simulated winds prevails over the specific humidity and temperature differences and leads to too large simulated turbulent heat fluxes for the largest values. This is relevant for our study, since climatological near-surface winds can influence the PAM and VMM mechanisms at play in this region (Spall 2007; Small et al. 2008; Chelton and Xie 2010). With regard to the role of model resolution, although HR heat flux values are slightly larger than LR for the highest deciles, no significant differences emerge from this analysis, since both HR and LR values are inside the ensemble spread.

b. *Characterization of synoptic atmospheric patterns over the GS*

In this section we analyze the composite maps obtained from the decile classification described in the previous section. We first focus on the description of the atmospheric circulation in terms of sea level pressure (SLP) and 10-m winds (vectors) in ERA5 for the 10 deciles (Fig. 4). The composite maps of SLP and 10-m winds are computed using daily anomalies with respect to the mean daily climatology. Only ERA5 is shown here as both models show results very similar to the reanalysis for these composite maps. Hereinafter we remove from the analysis the ERAI reanalysis since the goal of this study is to focus on the ARPEGE model and its performance with respect to the very recent ERA5 dataset. The first decile pattern (d1; Fig. 4), which corresponds to the lowest values of THF or the weakest air–sea exchange, shows positive SLP anomalies indicating anticyclonic conditions over the GS region. The anomalous flow near the surface related to this configuration is characterized by southwesterly winds flowing into the GS south of 40°N, bringing moist and warm air over the ocean, and northwesterly winds between 40° and 50°N and 50°–40°W over the Grand Banks area associated with cold air advection. The Grand Banks area is the northernmost part of the GS, and it can be seen as the confluence zone between the warm and salty GS current and the relatively cold and fresh water from the Labrador Current. When the ASII gets larger from d2 to d6, the anticyclonic conditions persist, although they get weaker as we go toward higher deciles. From d7 to d10, the SLP anomalies become negative over the GS. The 10th decile (d10; Fig. 4), which corresponds to the largest THF release, displays an intense cyclonic circulation over the GS, with anomalous northwesterly winds bringing cold and dry air into the GS, and warmer and moister southwesterly winds over the Grand Banks area. The importance of northwesterly winds associated with synoptic-scale disturbances for strong THF release events over the GS region is in accordance with the results found by Ogawa and Spengler (2019). In summary, the classification of the synoptic atmospheric patterns over the GS depending on the strength of air–sea interactions over the GS reveals two opposite anomalous atmospheric patterns, with anticyclonic conditions 60% of the time, and cyclonic conditions 40% of the days. As described in Parfitt and Czaja (2016), these atmospheric large-scale patterns are associated with a baroclinic waveguide propagating eastward across the GS (Chang et al. 2002). Their temporal evolution is around 7 days, which corresponds to the synoptic scales in the atmosphere.

It is important to note that both model configurations represent very well the decile patterns when compared with ERA5, although slight differences can be observed in terms of SLP amplitude. Note that these patterns are also very similar to the ones obtained by Parfitt and Czaja (2016) for ERAI.

In the following, we focus our analysis on the d1 and 10 composites for relevant variables only for ERA5 reanalysis. Since these two situations are extreme and opposite, this allows us to better identify the impact of synoptic conditions on the MABL processes. Composite maps are weighted [see Eq. (2)] to estimate the contribution of each decile to the time mean. Figure 5 shows the composite patterns in terms of near-surface wind divergence, precipitation, and vertical pressure velocity at 500 hPa in the wintertime mean and for d1 and d10.

Figures 5a–c show the near-surface wind divergence patterns, positive (negative) values indicate a wind divergence (convergence) at the surface. The mean pattern is characterized by a divergence of near-surface winds over the northern side of the SST front and a convergence along the warm side of the SST front (Fig. 5a). Over the warm side of the SST front, associated with the mean convergence zone, a band of enhanced precipitation is found in ERA5 (Fig. 5d). This enhanced precipitation is associated with intense vertical motions as shown by the mean vertical pressure velocity at 500 hPa (Fig. 5g). Indeed, in the upper atmospheric levels, the mean vertical pressure velocity at 500 hPa indicates mainly an ascent (negative values) along the warm side of the SST front, which is consistent with the wind convergence map shown in Fig. 5a.

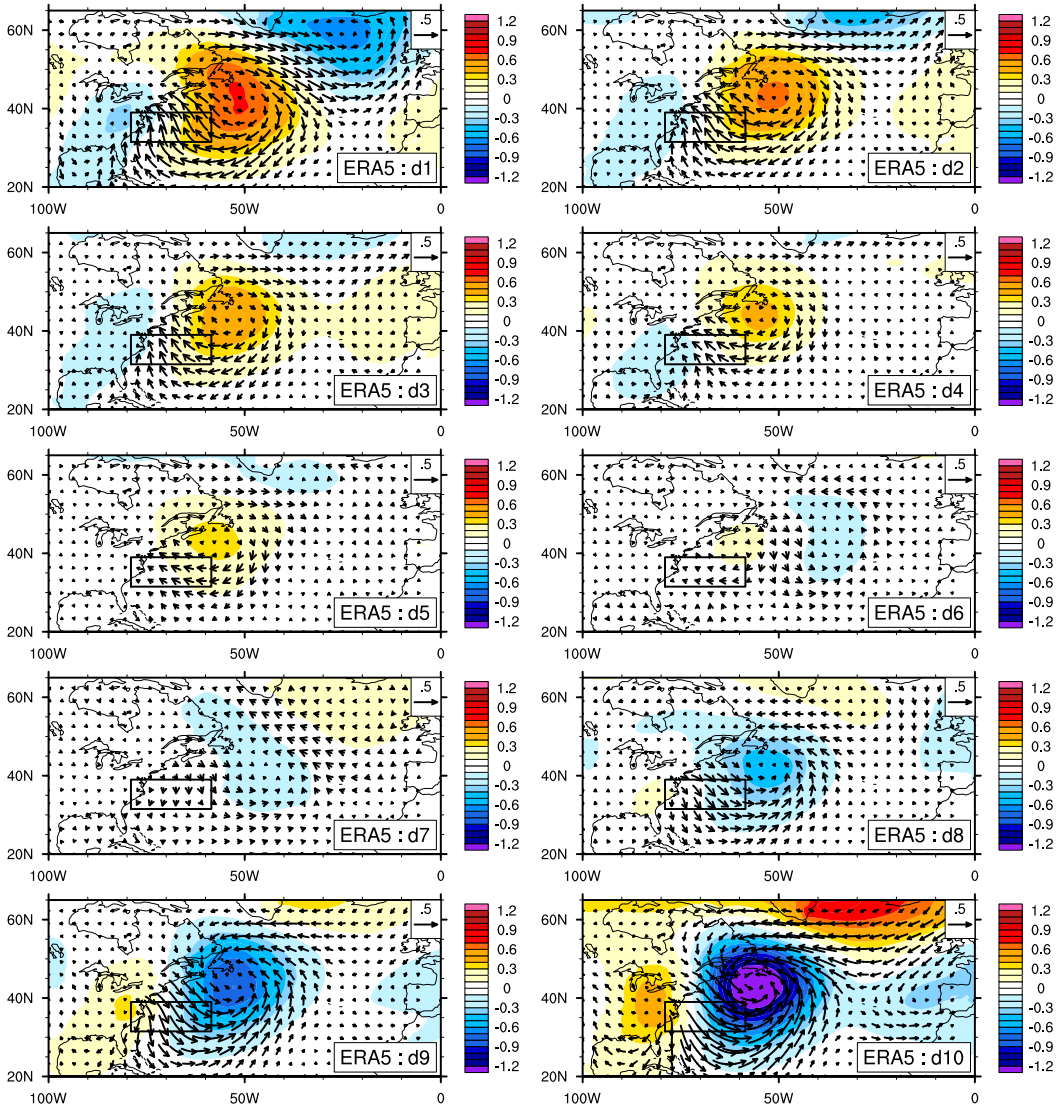

FIG. 4. Decile patterns (d1–d10) for ERA5 obtained from the ASII as explained in the text. Shading represents the SLP anomalies (hPa), and vectors correspond to 10-m wind anomalies ($m\,s^{-1}$; reference vector = $0.5\,m\,s^{-1}$).

The atmospheric situation associated with d1, which corresponds to anticyclonic anomalies over the GS, exhibits a strong convergence zone over the warm flank of the SST gradient west of 65°W and a strong divergence zone located over the Grand Banks area (Fig. 5b). A comparison between Figs. 5a and 5b indicate that under strong anticyclonic conditions over the GS region, the wind divergence or convergence is respectively enhanced or reduced in d1 relative to the time mean. Close to the coast, under weak cyclonic conditions, an area of convergence is associated with a band of enhanced precipitation (Fig. 5e). This precipitation feature contributes to approximately 20% of the time mean over that area and is consistent with a strong vertical motion upward at 500 hPa over this zone as shown by the vertical pressure velocity (Fig. 5h).

The near-surface wind divergence pattern for d10 displays an east–west convergence–divergence dipole between 30° and 45°N (Fig. 5c). It is characterized by enhanced divergence near the coast and enhanced convergence offshore east of 60°W. The precipitation pattern for d10 (Fig. 5f) shows strong values as compared with the time mean over the convergence zone, which accounts for approximately 20% of the total mean precipitation over that area. The pattern of vertical pressure velocity at 500 hPa is very different from the one obtained for d1. Notably, d10 is characterized by enhanced ascent over the convergence zone and enhanced downward motion near the coast (Fig. 5i).

To conclude, we have identified two opposite and extreme synoptic patterns over the GS related to the weakest and strongest air–sea interactions in terms of turbulent heat fluxes. We have shown that near-surface wind convergence and upward motion can occur at different locations in the GS region depending on these synoptic conditions. Next, we investigate

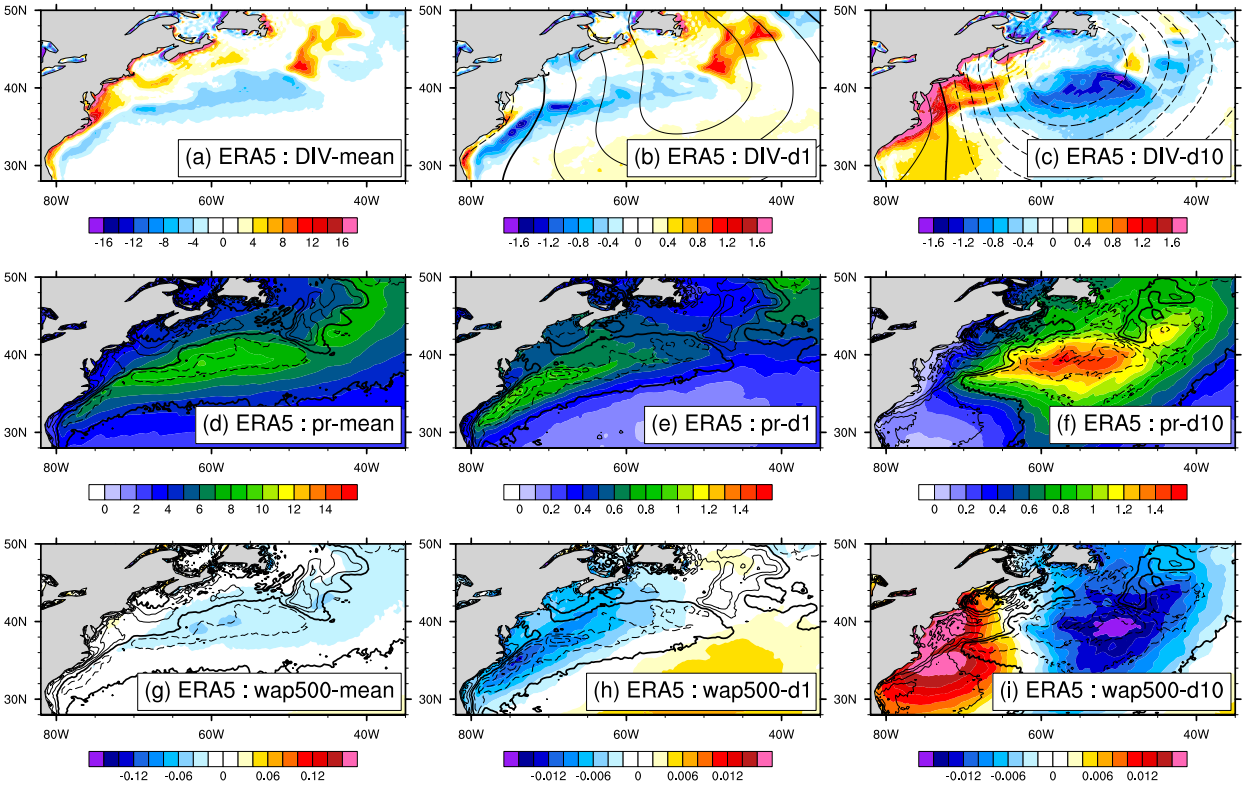

FIG. 5. Pattern for ERA5 of near-surface wind divergence (a) in the time mean, (b) for d1, and (c) for d10. The shading represents the divergence ($\times 10^{-6}\,s^{-1}$), and the contours indicate the SLP anomalies (every 0.2 hPa). (d)–(f) As in (a)–(c), but the shading is for precipitation (mm day^{-1}) and contours are for near-surface wind divergence ($\times 10^{-6}\,s^{-1}$). (g)–(i) As in (a)–(c), but shading is for vertical velocity pressure at 500 hPa (Pa s^{-1}) and contours are for near-surface wind divergence ($\times 10^{-6}\,s^{-1}$).

how the two ARPEGE configurations represent these features with respect to ERA5.

c. *Model evaluation*

Figure 6 shows the HR-LR and HR-ERA5 differences for the time-mean patterns. The divergence pattern is overall very similar in LR and HR. The negative signal near the coast indicates that the coastal divergence is located farther from the coast in LR. HR also shows weaker convergence eastward over the ocean (Fig. 6a). The precipitation band is slightly shifted north in HR (Fig. 6c) and the vertical motion is reduced in HR when compared with LR (Fig. 6e). Divergence patterns in models are very similar in comparison with ERA5, but both models overestimate surface wind divergence (Fig. 6b), whereas precipitation and vertical ascent are underestimated with respect to ERA5 (Figs. 6d,f).

For the d1 and d10 composites, HR exhibits larger positive or negative SLP anomalies near the coast in d1 or d10, respectively, than LR (Figs. 7a and 8a). This is consistent with the pressure centers that are shifted toward the North American coast in HR, which might be partly due by a different representation of land–sea contrast and associated pressure gradients in HR. Further, the amplitude of the SLP anomalies over the GS is larger by about 20% in HR when compared with ERA5 for both d1 and d10 (Figs. 7a and 8a).

In d1 the convergence zone near the coast is enhanced in HR, together with more precipitation and stronger vertical ascent (Figs. 7c,e,g). The convergence near the coast associated to d1 is overestimated in models relative to ERA5, and this is consistent with increased precipitation and vertical ascent very close to the coast (Figs. 7d,f,h). For d10, convergence is stronger in HR over the northern part of the extended convergence area (Fig. 8c). This leads to more precipitation and enhanced vertical ascent in HR (Figs. 8e,g). The fact that near-surface convergence is overestimated in models can be related to stronger simulated winds in ARPEGE (Fig. 3). However, this feature is not coherent with increased precipitation in ERA5 for d10. Further analysis reveals that only the convective precipitation is underestimated in both models, which reveals that convection parameterizations in ARPEGE can be at play.

d. *Decile contributions to the time-mean divergence*

We quantify the contribution of each decile to the time-mean divergence and convergence patterns for ERA5 and the models by applying the method introduced by Parfitt and Czaja (2016). The method consists of reconstructing the time-mean pattern by performing a linear regression analysis between the time mean and the decile patterns, as illustrated in Fig. 9 for ERA5. In Parfitt and Czaja (2016) this method was used to

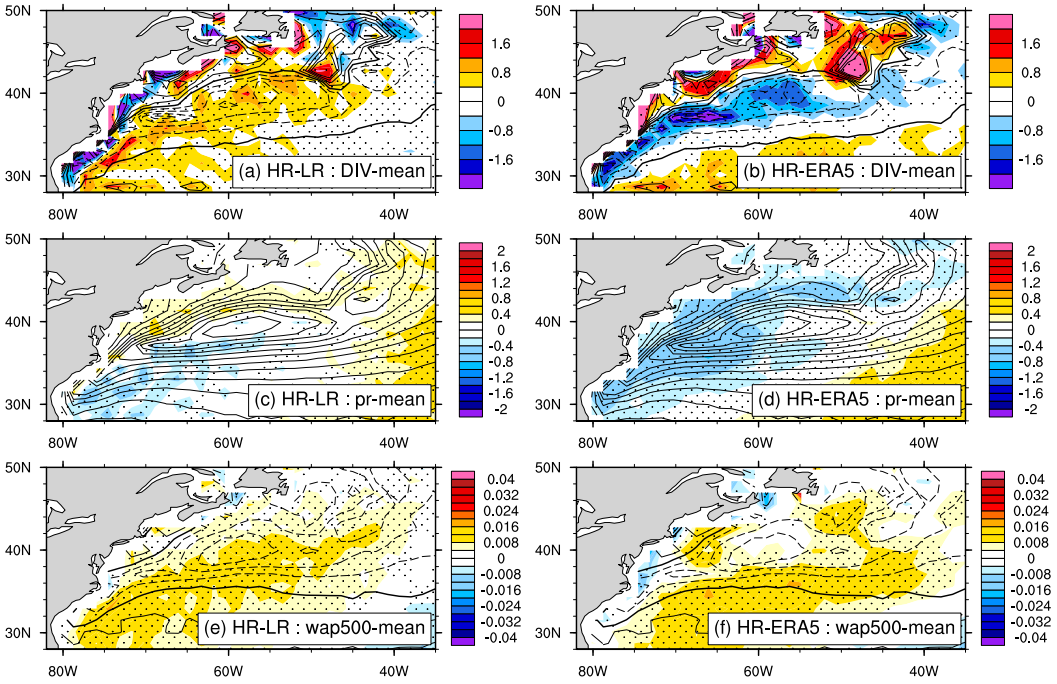

FIG. 6. Pattern of differences for the time mean of near-surface wind divergence for (a) HR− LR and (b) HR − ERA5. The shading represents the differences ($\times 10^{-6}\,s^{-1}$), and the contours indicate the near-surface wind divergence of HR (every $2 \times 10^{-6}\,s^{-1}$). (c),(d) As in (a) and (b), but shading is for precipitation (mm day^{-1}) and contours are for precipitation of HR (every 0.5 mm day^{-1}). (e),(f) As in (a) and (b), but shading is for vertical velocity pressure (Pa s^{-1}) and contours are for vertical velocity pressure of HR (every 0.01 Pa s^{-1}).

compute the decile contributions for variables such as vertical pressure velocity, which can take positive and negative values. Here we apply a similar analysis to the near-surface wind divergence/convergence. Since the divergence values can cancel out when computing the time mean, we separate the positive (Fig. 9a) and negative (Fig. 9b) divergence values before performing the linear regression. To have more robust decile patterns, we consider separately the three lowest (d1–d3) and the three highest (d8–d10) deciles, keeping in mind that each of these groups is associated with similar atmospheric circulation regimes (Fig. 4). The percentage of explained variance of the time mean is measured by the square of the correlation coefficient R^2 obtained from the regression (Fig. 10). For the LR and HR models, the regression is computed using the ensemble mean patterns.

For positive values of the wind divergence, the three highest deciles show the most important contribution to the time mean (Fig. 10a), with more than 80% of the total contribution explained in the models and ERA5. The lowest deciles contribute in a lesser extent to the time-mean divergence with around 30% for ERA5 and around 20% for HR and LR. As in Parfitt and Czaja (2016), we can then combine the three lowest and three highest deciles in order to perform a reconstruction of the time mean. This reconstruction is called "combined" in Fig. 10. Combined reconstruction explains more than 90% of the time mean for positive values of the wind divergence (see also the scatterplot in Fig. 9a). This result confirms that the wind divergence pattern over the GS can be mostly explained by the occurrence of two opposite synoptic patterns. The cyclonic events (d8–d10), which are associated with the strongest THF release to the atmosphere, provide the largest contribution to the time-mean wind divergence (for the positive values).

For the negative values of wind divergence (the convergence), the time mean is also mostly explained by the highest deciles, which contribute to about 70%–80% of the mean (Figs. 10b and 9b). The lowest deciles show again a lower contribution, with values between 60% for ERA5 and 40% for HR and LR. This suggests that the role of the lowest deciles is slightly underestimated in the models for positive and negative divergence. Again, the combined reconstruction for the wind convergence explains more than 90% of the mean, which corroborates the important role of synoptic disturbances in shaping the time-mean convergence in the GS.

The linear regression analysis was repeated by considering interpolated fields rather than fields over their original grids. HR and ERA5 were interpolated on the LR grid in order to determine whether the results above can be affected by the larger number of grids points in the domain in ERA5 and HR relative to LR. The linear regression analysis shows slightly different values of R^2 from interpolated fields (not shown) but the conclusions about the decile contributions are unchanged.

This analysis suggests that the near-surface wind divergence over the GS can be reconstructed from a combination of anticyclonic and cyclonic synoptic patterns propagating eastward over the GS. Furthermore, although the frequency of occurrence of cyclonic disturbances (40%) is lower than that of

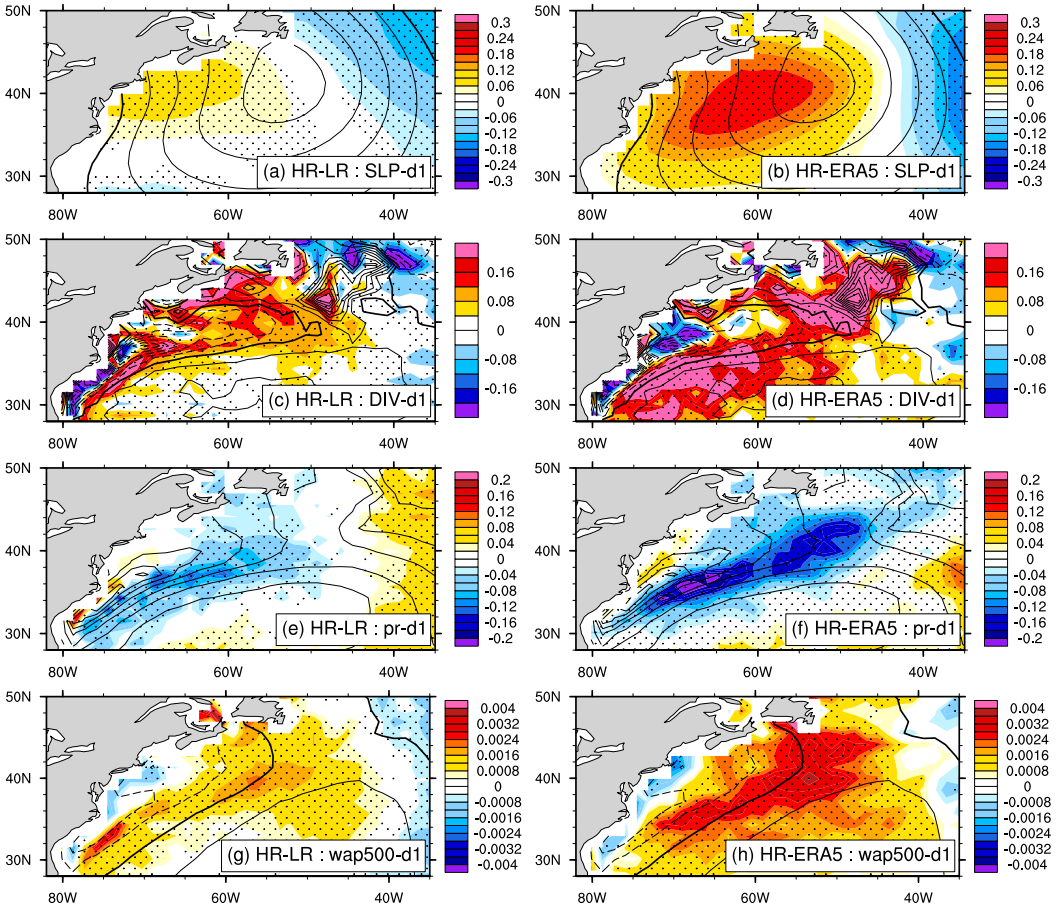

FIG. 7. Pattern of differences for d1 of SLP anomalies for (a) HR − LR and (b) HR − ERA5. The shading represents the differences (hPa), and the contours indicate the SLP anomalies of HR (every 0.2 hPa). (c),(d) As in (a) and (b), but shading is for near-surface wind divergence ($\times 10^{-6}\,s^{-1}$) and contours are for near-surface wind divergence of HR (every $0.2 \times 10^{-6}\,s^{-1}$). (e),(f) As in (a) and (b), but shading is for precipitation (mm day^{-1}) and contours are for precipitation of HR (every 0.1 mm day^{-1}). (g),(h) As in (a) and (b), but shading is for vertical velocity pressure (Pa s^{-1}) and contours are for vertical velocity pressure of HR (every 0.004 Pa s^{-1}).

anticyclonic ones (60%), the large contribution of the cyclonic perturbations to the time-mean divergence/convergence suggests they exert an important role in modulating the MABL processes. In the next section we investigate the VMM and PAM mechanisms associated with the divergence/convergence patterns obtained for the time mean and the deciles. We will particularly focus on a comparison between models and reanalysis for the two most extreme deciles.

4. Importance of the VMM and PAM mechanisms for the time mean and the deciles

a. Role of the VMM

Before focusing on the role of the VMM in extreme decile configurations, we analyze all the decile patterns for the DW_SST (Fig. 11) for ERA5 reanalysis. According to the time-mean pattern of the DW_SST, the VMM on average occurs over the two main divergence zones of the GS: the first one located along the North American coast, and the second one over the Grand Banks area. In winter, the climatological large-scale atmospheric circulation is mainly characterized by a northwesterly flow of continental air that crosses the SST front from its cold to warm side. This results in a positive DW_SST that is associated with an acceleration of the surface winds over warm waters through vertical mixing. This leads to near-surface divergence of the winds close to the coast and over the Grand Banks area (Chelton and Xie 2010). These spatial features are in agreement with previous studies (Takatama et al. 2015; O'Neill et al. 2017). The time-mean DW_SST is positive almost everywhere except in few localized areas over the southern and northern part of the GS current. The composite maps for lower deciles (d1–d3; Fig. 11) show a large and positive DW_SST over the divergence zone near the Grand Banks. This can be explained by the anticyclonic circulation associated with lower deciles (Fig. 4), which yields anomalous northwesterly wind flow eastward from a colder ocean in the north toward warmer waters (Fig. 4), leading to near-surface

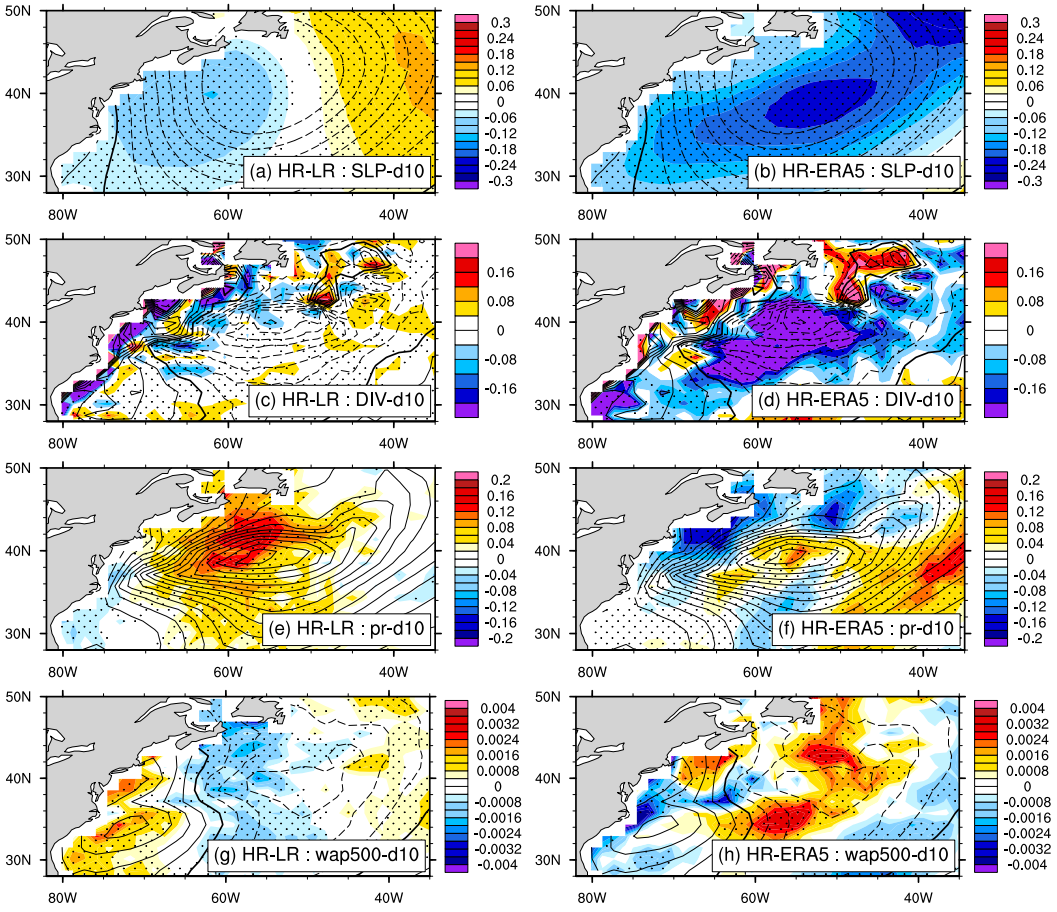

FIG. 8. As in Fig. 7, but for d10.

divergence in this area through enhanced vertical mixing. A weak negative DW_SST is also found over the convergence zone of the GS. This could be explained by the southeasterly winds that cross the SST gradient from warm to cold waters, yielding to near-surface convergence by a weakening of the vertical mixing. This negative area of DW_SST is canceled out by other deciles' contributions when computing the time mean. The intermediate decile patterns (d4–d7; Fig. 11) are very similar to the time-mean pattern in Fig. 11. For higher deciles (d8–d10; Fig. 11), cyclonic anomalies (Fig. 4) lead to an enhancement of the surface westerly winds at the surface over the warmer waters, creating a wind divergence. For the highest deciles (d10; Fig. 11), weak negative values for the DW_SST are even found over a small convergence area near the Grand Banks. This can be explained by the anomalous easterly winds blowing from the warm sector of the SST front, which weaken over colder waters, leading to a convergence of the wind.

We analyze how models represent the time mean and extreme decile patterns for the DW_SST described above (Fig. 12). The time mean of the DW_SST is correctly represented by both models (Figs. 12a–c), although the negative values of DW_SST are not present in LR. This indicates that LR does not represent smaller-scale features associated with the VMM such as the negative DW_SST. For the d1, models represent very well the large-scale features of the DW_SST pattern, suggesting that the VMM is present (Figs. 12d–f). Nevertheless, the amplitude of the DW_SST is underestimated in LR, and we also notice an absence of the narrow zone of positive DW_SST at Cape Hatteras in LR, indicating that finer-scale processes are not correctly simulated over this region at this coarse resolution. Indeed, spatial resolution in LR does not allow representation of this narrow feature at a 140-km grid. The d10 pattern of DW_SST is also well simulated by models, although once again LR underestimates the amplitude of the pattern (Figs. 12g–i). This is in accordance with the results found in terms of SST gradient, where LR has shown to have reduced amplitude of SST gradient in comparison with HR and ERA5 (Fig. 1c).

Based on our cluster analysis we have examined the role of VMM for extreme conditions of air–sea interactions over the GS. For weak values of the THF, the VMM mostly occurs over the divergence zone over the Grand Banks area. For large THF, the signature of the VMM is greatest along the North American coast, where the wind surface divergence develops. The results are very similar in the models and in

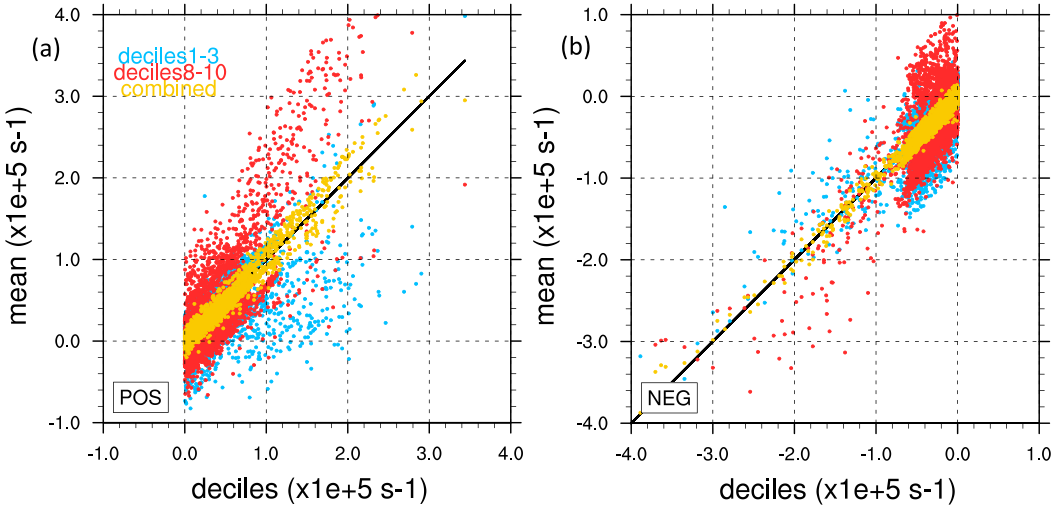

FIG. 9. Scatterplot between the time-mean divergence (vertical axis) and deciles 1–3, deciles 8–10, and their combination (horizontal axis) for (a) positive values and (b) negative values . The diagonal line that represents equality is also shown. Here, x1e+5 indicates multiplication by 10^5.

ERA5, although some smaller-scale structures are not present in LR because of its coarser resolution.

To better quantify which deciles contribute most to the time mean, we show in Fig. 10 the percentage of variance explained by the three lowest and three highest deciles of DW_SST for the time mean using the same regression analysis as described in section 3d. We again separate positive and negative values of the DW_SST. The regression analysis shows that, for both positive and negative values of the DW_SST, most of the time mean is explained by the three highest deciles (Figs. 10a,b), with more than 90% of the mean. The three lowest deciles have a smaller contribution, between 20% for LR and 50% for HR and ERA5. Combining the highest and lowest deciles leads to a reconstruction that explains more than 90% of the time mean. This indicates that the climatological VMM features are mainly explained by extreme conditions in THF.

b. *Role of the PAM*

Figure 13 shows the decile patterns of LAP(SLP) and contours of near-surface wind divergence for ERA5. The time-mean pattern indicates that positive or negative values for LAP(SLP) are associated with wind convergence or divergence

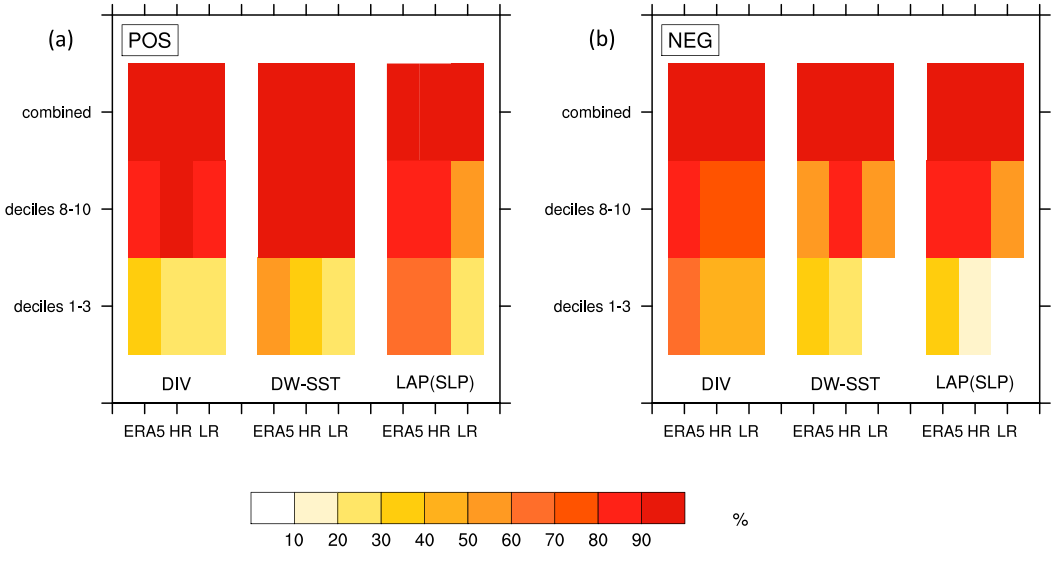

FIG. 10. Percentage of time mean explained (%) obtained from the squared correlation coefficient between the time mean and decile patterns for divergence, DW_SST, and LAP(SLP): for (a) positive values and (b) negative values. As explained in the text, the correlation is computed separately for the lowest deciles, the highest deciles, and their combination.

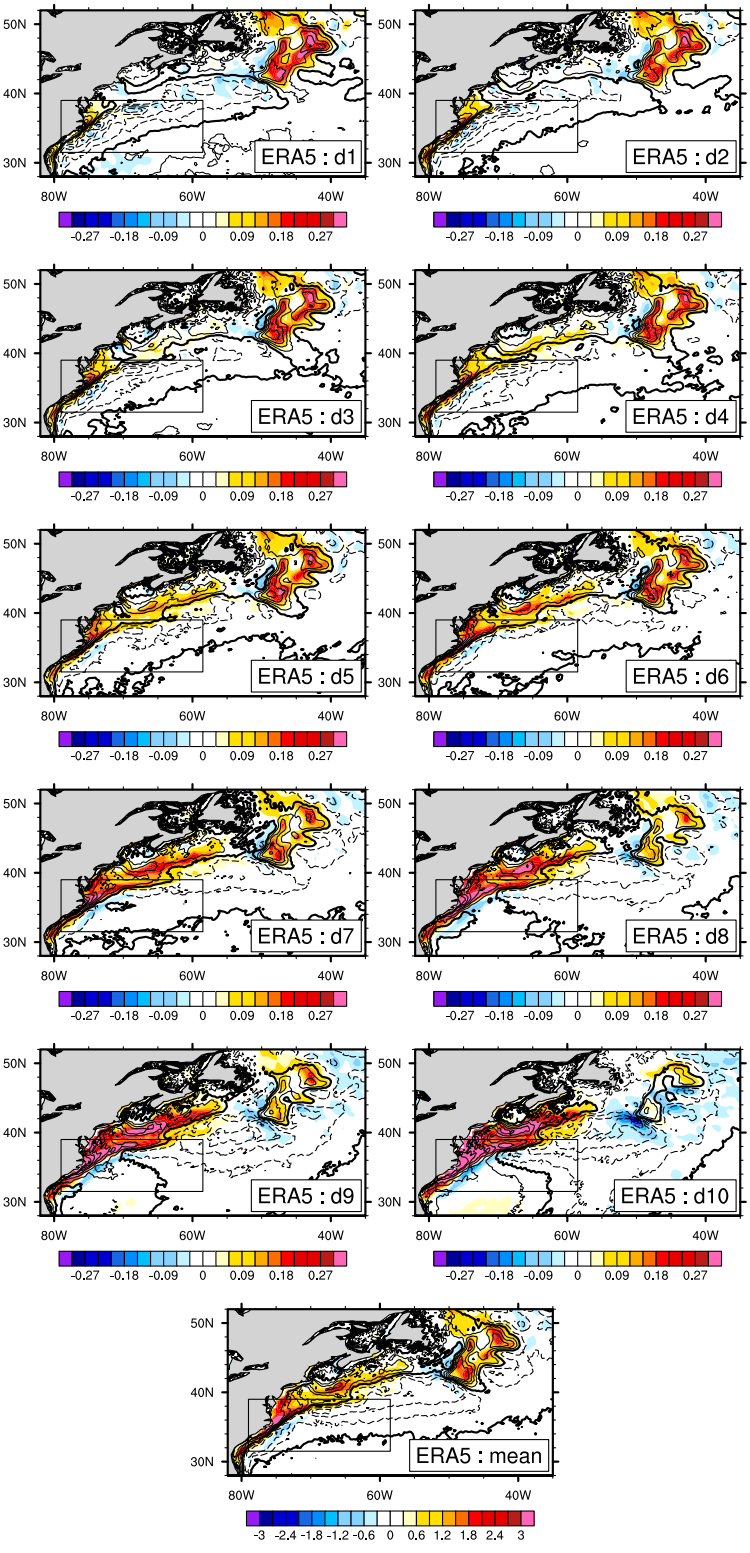

FIG. 11. Decile patterns (d1–d10) and the mean for ERA5 obtained from the ASII. Shading represents the DW_SST [°C $(100\,\mathrm{km})^{-1}$], and contours represent near-surface wind divergence ($\times 10^{-6}\,\mathrm{s}^{-1}$).

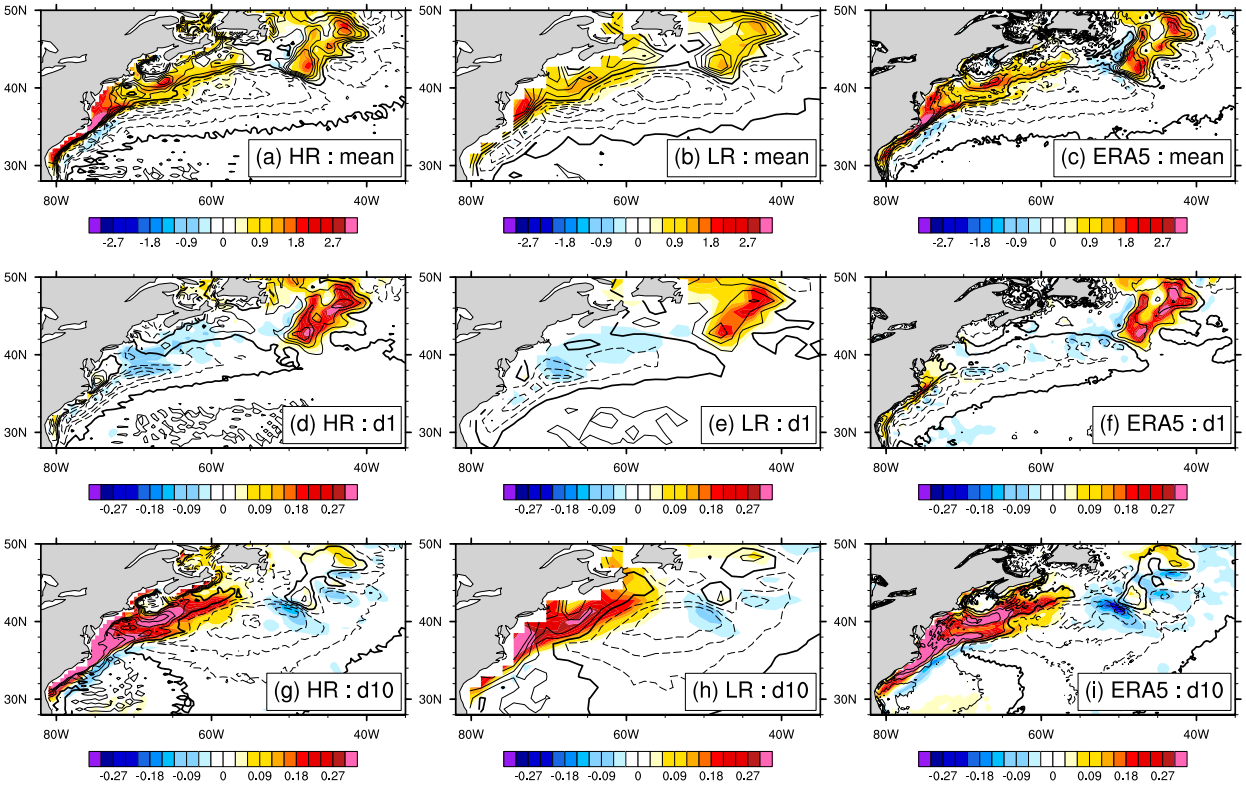

FIG. 12. Patterns of the time-mean DW_SST for (a) HR, (b) LR, and (c) ERA5. The shading represents the DW_SST [°C (100 km)$^{-1}$], and the contours indicate the near-surface wind divergence (from -8×10^{-6} to 8×10^{-6} s^{-1} every 2×10^{-6} s^{-1}). (d)–(f) As in (a)–(c), but for the d1 pattern. (g)–(i) As in (a)–(c), but for the d10 pattern.

near the surface, respectively, consistent with Minobe et al. (2008). At low deciles (d1–d3; Fig. 13), strong negative values of LAP(SLP) are found over the Grand Banks area, whereas positive LAP(SLP) is present over the warm flank of the SST front. When an anticyclone is crossing the GS, the anomalous atmospheric circulation (d1–d3; Fig. 4) is associated with wind divergence over the anticyclone center. This leads to a generalized reduction of the GS convergence zone around 60 W with respect to the time mean. The convergence zone is then located near the coast for lower deciles [LAP(SLP) $>$ 0]. Moreover, anticyclonic conditions yield to divergence increase over the Grand Banks area [LAP(SLP) $<$ 0] with respect to the time mean. The patterns associated with d4–d7 in Fig. 13, which correspond to neutral conditions, are very close to the time-mean pattern. Higher deciles (d8–d10; Fig. 13) show intense positive LAP(SLP) values over the extended convergence zone. Cyclonic circulation (d8–d10; Fig. 13) is associated with strong wind convergence over the GS, leading to an intensification of the convergence near the cyclone center (40°N, 60°W) where LAP(SLP) $>$ 0. On the other hand, the divergence area over the Grand Banks is drastically reduced for higher deciles with respect to the time mean. The highest decile (d10) presents a strong signal of positive LAP(SLP), with the largest contribution to the GS main convergence zone (20%). O'Neill et al. (2017) argued that extreme wind divergence events associated with atmospheric disturbances leave their considerable imprints on the mean fields. According to this argument, a few passing cyclones would leave significant signatures on the LAP(SLP) for d10. To check this hypothesis, we have isolated the days of extreme LAP(SLP) values within d10. We have defined extreme LAP(SLP) events as those days exceeding one standard deviation of the full d10 distribution. The results (not shown) indicate that these days, which account for 13% of the d10 data, represent 40% of the total d10 signal. This confirms an important role of strong cyclonic events in LAP(SLP) for higher deciles. Furthermore, the composite approach used in this study is an average over many events, which differ in the location and intensity of the pressure centers. Therefore, the good spatial correspondence between LAP(SLP) and wind divergence found for the d10 composite pattern would not necessarily be valid for each day of d10. To investigate this issue, we have computed the spatial correlation between LAP(SLP) and wind divergence for each of the 163 days belonging to d10 in ERA5, using an 8° latitude and longitude box centered over the SLP minimum. We find that 63% of the days present a spatial correlation larger than the one obtained for the d10 composite pattern in Fig. 13 (not shown). This indicates that the good correspondence between LAP(SLP) and surface wind divergence cannot be explained by only few isolated events.

Our analyses show that atmospheric disturbances can modulate the PAM through changes in the anomalous atmospheric

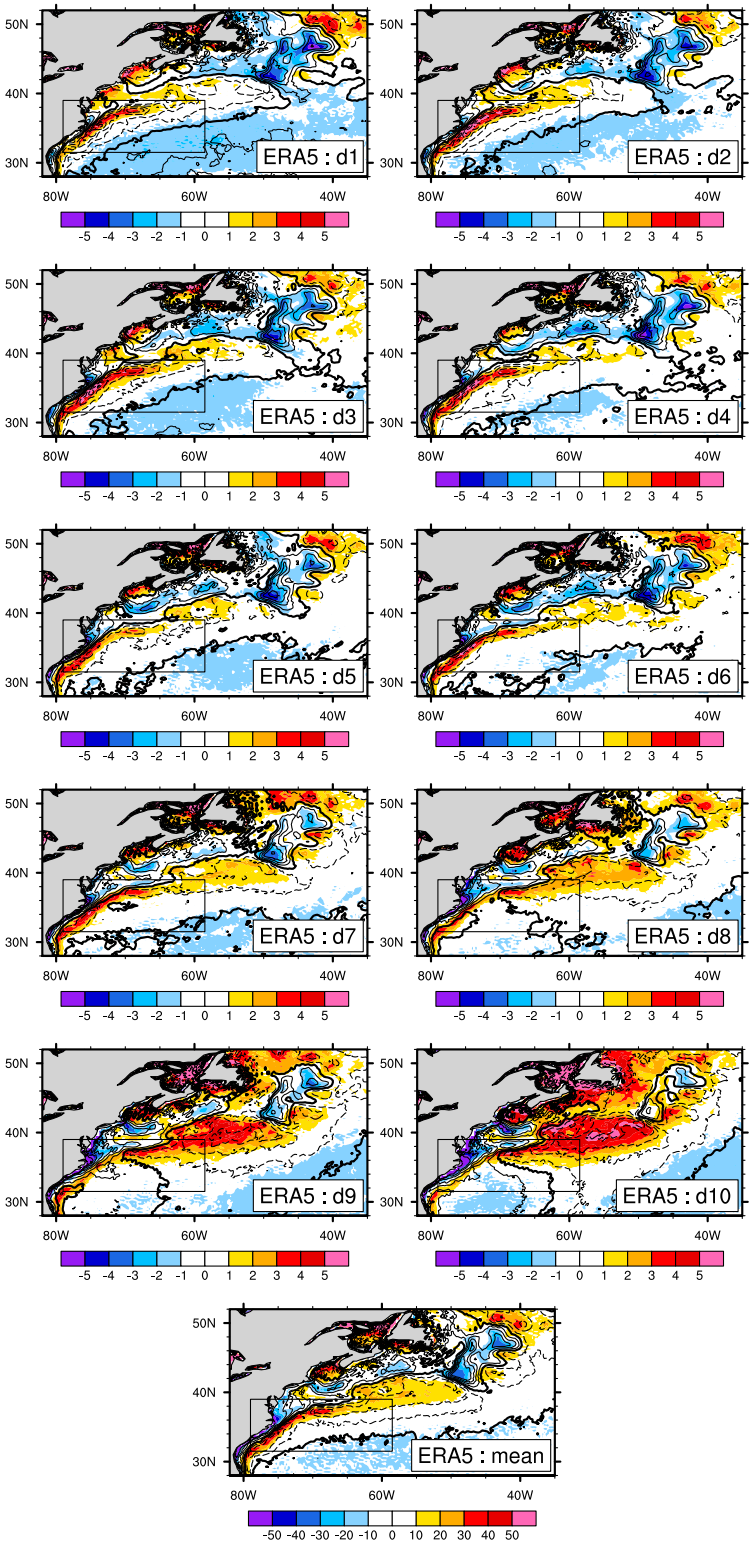

FIG. 13. As in Fig. 11, but shading represents the LAP(SLP) ($\times 10^{-10}$ Pa m^{-2}), and contours represent near-surface wind divergence ($\times 10^{-6}$ s^{-1}).

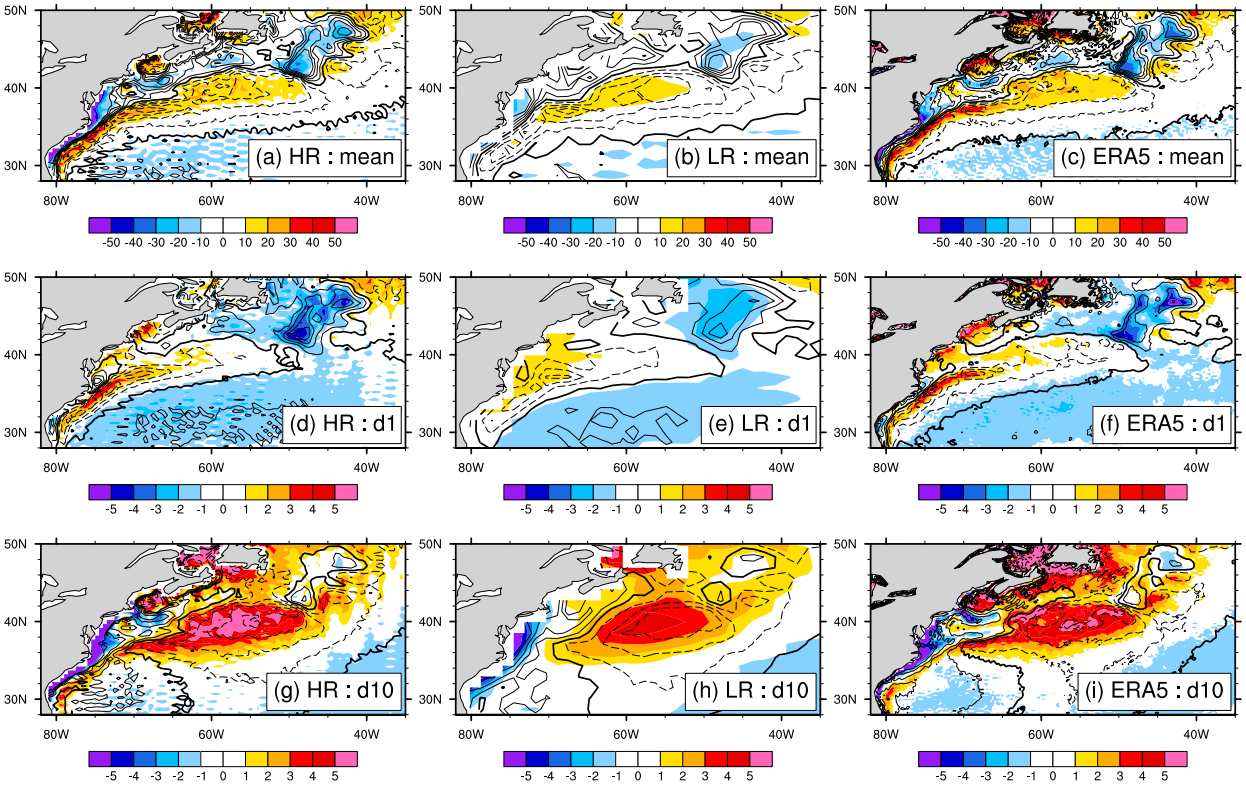

FIG. 14. As in Fig. 12, but the shading represents the LAP(SLP) ($\times 10^{-10}$ Pa m^{-2}).

circulation over the GS. Basically, anticyclones are associated with strong negative LAP(SLP) over the Grand Banks and negative LAP(SLP) very close to the coast. On the other hand, the cyclones imprint leads to a wide area of positive LAP(SLP) offshore. These two opposite situations do not cancel out in the time mean.

We examine how models reproduce the time mean and extreme decile patterns of LAP(SLP) (Fig. 14). A spatial noise is noticeable in the HR patterns. This is due to the Gibbs phenomenon, which is very common in spectral models like ARPEGE (Yessad 2015). The Gibbs effect is amplified when computing high-order derivatives like for the LAP(SLP), and also in high-resolution models. For the time mean (Figs. 14a–c), the large-scale pattern of LAP(SLP) is quite similar in the models and ERA5, although the values of LAP(SLP) in LR are lower than in the HR model. For the extreme deciles (Figs. 14d–i), the same correspondence between the LAP(SLP) and wind divergence is found in both models and in ERA5, but the magnitude of the anomalies is smaller in LR. This is in accordance with the results found for the SST gradient, where LR was shown to have weaker SST gradient in comparison with HR and ERA5 (Fig. 1c). An interesting feature is the spatial shift observed for d10 between the maxima of LAP(SLP) and near-surface convergence, this feature will be discussed in more detail in the next section.

The regression analysis in Fig. 10 indicates that for both positive and negative values of LAP(SLP), the largest contribution is provided by the three highest deciles, with more than 80% of the time mean in HR and ERA5. The values are slightly lower in LR. The combined reconstruction using the three lowest and three highest deciles captures almost all the time-mean field, which highlights the importance of extreme air–sea interactions conditions for the PAM.

c. *Contribution of the VMM and PAM for each decile*

We quantify the relative contribution of the VMM and PAM to the wind divergence/convergence for each decile of the ASII. As in previous studies, the importance of these mechanisms is measured by the degree of spatial correspondence between the DW_SST (for the VMM) or the LAP(SLP) (for the PAM) and the near-surface wind divergence/convergence. We compute the spatial correlation between the DW_SST and the near-surface wind divergence in one case, and between the LAP(SLP) and the near-surface wind divergence in the other case, for each decile and for the time mean separately. We consider the spatial domain 30°–48°N, 40°–80°W, as in Minobe et al. (2008). The percentage of explained variance defined by the square of the correlation coefficient is shown Fig. 15. For the time mean, the VMM explains about 30% of the total wind divergence in ERA5 (Fig. 15a). This contribution is overestimated by the models, in particular HR. The largest percentage of variance can be explained by the three highest deciles (d8–d10). This suggests an important role of the VMM during cyclonic atmospheric conditions over the GS.

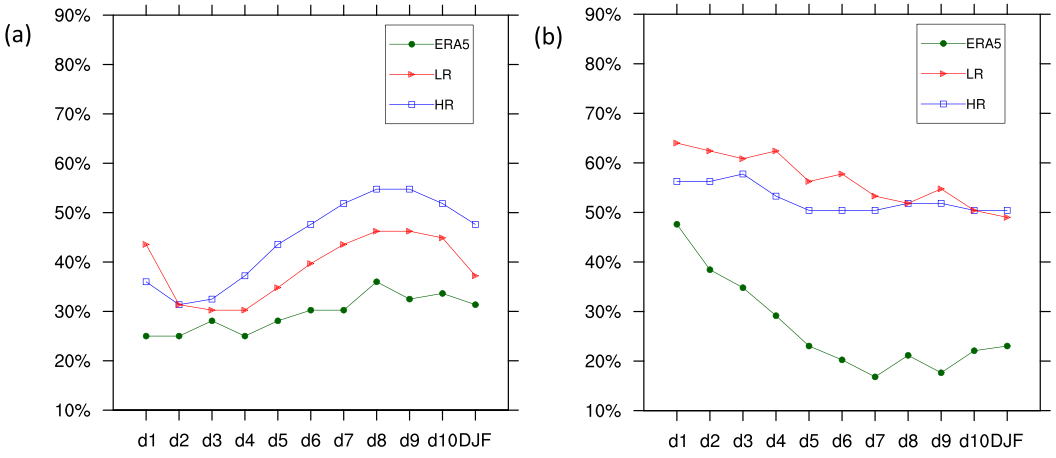

FIG. 15. Percentage of variance explained (%) obtained from the squared correlation coefficient between each decile patterns of the surface wind divergence and (a) DW_SST and (b) LAP(SLP). Results are also shown for the DJF mean. Values are shown for HR (blue), LR (red), and ERA5 (green).

In contrast, the PAM seems to play a more important role for the lowest deciles, with more than 50% of the variance explained for d1–d3 in the models (Fig. 15b). This percentage is lower for ERA5, which shows decreasing variances as the deciles increase and variances up to 30% lower than the model, in particular for the highest deciles.

Figure 15 indicates that the LR and HR models tend to overestimate the role of the VMM and PAM on the near-surface wind divergence over the GS. Note that the percentage of explained variance illustrated in Fig. 15 is computed from the original grids but the conclusions remain unchanged when using interpolated fields.

Our findings indicate that VMM predominates over the SST front when cyclonic perturbations cross the GS region, with a more limited role for the PAM under these cyclonic conditions. This is consistent with previous studies that pointed to weaker winds environments to be more favorable for the PAM to develop (Spall 2007; Shimada and Minobe 2011). Lower-order deciles are associated with weaker near-surface winds regimes as the prevailing anomalous winds are southeasterly (opposite to the westerly mean flow), and the variance explained by the PAM is indeed larger in the models and ERA5 for the lowest deciles. However, the results of Fig. 15 should be considered with caution. Indeed, the maximum of near-surface wind convergence in Figs. 14g–i is shifted eastward with respect to the maximum of LAP(SLP) in the models and in ERA5. This shift appears also for the time mean (Figs. 14a–c), but to a lesser extent. This spatial shift can partly explain the lower correlation found between LAP(SLP) and the wind divergence for higher deciles (Fig. 15b).

Previous studies reported that at monthly time scale, the maximum of spatially high-pass filter SLP, characterized by LAP(SLP), is collocated with the maximum of wind convergence (Tokinaga et al. 2009; Minobe et al. 2008, 2010). In these studies, the spatial correspondence between the LAP(SLP) and the divergence/convergence was explained by the simplified MABL model from Lindzen and Nigam (1987). This MABL model was developed for steady flows, which assumes that the tendency of the near-surface wind divergence/convergence field is zero. In this case, the terms of advection and deformation in the divergence equation can be neglected, and the remaining contributing terms are the LAP(SLP) and the vertical turbulent stress. It can be shown that under the steady flow approximation, the wind divergence/convergence is proportional to LAP(SLP) (Minobe et al. 2008), which point to the latter to be the main contributor to the wind divergence. However, if the steady flow assumption cannot be applied, the other terms in the divergence equation can play a non-negligible role. By construction, d1 and d10 are not at the equilibrium, unlike the time mean. This means that the tendency of the wind divergence/convergence equals zero for the time mean but not for the deciles (not shown). This indicates that, even if the VMM and PAM are the main contributors of air–sea interactions in the GS, other physical processes should be taken into consideration to understand the mechanism driving the near-surface wind divergence in the presence of synoptic perturbations, since the latter cannot be considered as steady regimes. The GS region is particularly complex for the understanding and quantification of the role of VMM, PAM, and other mechanisms, such as advection and deformation, in shaping the near-surface wind divergence, since synoptic disturbances are almost always present over this zone (section 3b; Fig. 4). Clustering analysis performed at daily time scale, such the one proposed in the present study, used to isolate a particular atmospheric configuration, have revealed to be an efficient and promising approach to better understand the air–sea interactions over SST fronts and the importance of the different mechanisms at play in the MABL (O'Neill et al. 2017; Masunaga et al. 2020a,b).

5. Summary and conclusions

In this study, we investigated the mechanisms at play in the MABL response to the SST front in the Gulf Stream. The

VMM and PAM mechanisms have been suggested to be mainly responsible for generating divergence and convergence of the near-surface wind over this region. However, there has been some debate about their relative importance in shaping the convergence, and other mechanisms were recently put forward to play an important role.

In terms of turbulent heat fluxes, both ARPEGE configurations overestimate the winter mean of the latent and sensible heat fluxes over the GS with respect to ERA5. We show that this can be explained by an overestimation of the extreme values of turbulent heat fluxes, both latent and sensible, which is coherent with stronger simulated winds over the region. However, increasing the resolution in the ARPEGE model seems to have little effect on the amplitude of the turbulent heat fluxes for this region. This overestimation of the THF over the ocean is a bias reported in the ARPEGE atmospheric model (Roehrig et al. 2020). This bias is reduced when ARPEGE is running in coupled mode.

Using a clustering approach in which we decomposed the PDF of the turbulent heat fluxes over the GS into deciles using daily values, we investigated the role of the VMM and PAM for extreme conditions of THF. Our analysis was based on the ARPEGE v6 atmospheric model forced by observed SSTs over the 1950–2014 period. To investigate the impact of atmospheric horizontal resolution typically used in state-of-the-art coupled climate models, on the representation of air–sea interactions in the GS, we analyzed two configurations of the model that only vary in terms of their horizontal resolution (140 km for the LR model; 50 km for the HR model). For each model we used an ensemble of 10 members. The results were compared with the recently available high-resolution ERA5 reanalysis.

Through a composite analysis, the patterns of SLP and near-surface winds corresponding to low and large THF exchange have been obtained. These patterns represent the atmospheric disturbances crossing the GS region from west to east, embedded in the baroclinic waveguide, with an alternation of anticyclonic (low THF) and cyclonic (high THF) circulations. This decile method was first implemented by (Parfitt and Czaja 2016) to highlight the importance of synoptic disturbances in shaping air–sea interactions over the GS. We showed that the atmospheric features in terms of SLP, precipitation, and vertical ascent associated with the decile patterns are well simulated by the LR and HR models when compared with ERA5, and the effect of the model resolution was found to be relatively small. Our results are consistent with other studies performed within the H2020-PRIMAVERA project, which use the HighResMIP experiments. Bellucci et al. (2021) and Tsartsali et al. (2021, manuscript submitted to *Climate Dyn.*) have studied the impact of model resolution on the representation of air–sea interactions over the Gulf Stream from experiments performed with coupled models. They conclude that the improvement of the VMM, PAM, and turbulent exchange processes is clear for climate models with an eddy-permitting ocean. However, this improvement is moderate with respect to LR models, and for example for the PAM the impact of the resolution is less clear. They also find that coupled models operating at similar resolutions in the atmosphere and in the ocean show the major improvements.

We find that synoptic deciles patterns modulate the time-mean divergence of the near-surface wind by influencing locally the zones of divergence or convergence over the GS. In particular, anticyclonic circulations associated with weak air–sea interactions yield divergence over the Grand Banks area and convergence near the coast along the Cape Hatteras. On the other hand, cyclonic circulations associated with strong air–sea interactions are characterized by strong divergence near to the North American coast and strong convergence eastward. Using a regression analysis, we further showed that the highest deciles provide the largest contribution to the time mean for the divergence of the near-surface wind. We showed that the time-mean near-surface divergence could be reconstructed using only the three lowest and three highest deciles, which represent 60% of the total number of days, which highlights the importance of synoptic perturbations in the time-mean divergence field.

Our decile classification also revealed to be an efficient approach for further understanding the importance of the VMM and PAM mechanisms inside the GS region. Under the anticyclonic conditions occurring over the GS and associated with weak THF (weakening of westerly flow, d1–d3), both mechanisms act over the Grand Banks area, generating a surface divergence of the surface wind over that region. For cyclonic conditions over the GS and associated with strong THF (strengthening of westerly flow; d8–d10), the VMM mostly occurs near the coast over the maximum of the SST gradient. This can be explained by the strong and cold winds blowing from the continent, which are enhanced when crossing the cold-to-warm SST gradient, inducing wind divergence. The PAM is mostly associated with the wide convergence zone located east of 60°W during cyclonic conditions as revealed by our analysis. Nevertheless these results must be interpreted with caution, because the separation between the PAM and atmospheric disturbances at synoptic time scales remains challenging (O'Neill et al. 2017; Parfitt and Seo 2018; Masunaga et al. 2020a,b).

We showed using a regression analysis that the largest contribution of the VMM and PAM mechanisms to the time mean occurs during the cyclonic perturbations associated with large THF. Further, the degree of spatial correspondence between the divergence/convergence field and the DW_SST on one hand and the LAP(SLP) on the other hand revealed that the VMM contributes more to the divergence/convergence during cyclonic conditions above the main convergence zone. The role of the PAM is less clear for cyclonic conditions, since a spatial shift is found between the maximum of LAP(SLP) and the convergence, indicating that the linear links between these two variables are not evident in this case. Here we argue that these results should be treated with caution. Indeed, by definition, the decile patterns are not steady flows. In this case, the simplified MABL model from Lindzen and Nigam (1987) could present some limitations.

ARPEGE models simulated very well all of the features and processes discussed above. Nevertheless, the VMM and PAM are underestimated in LR, which suggests a role of the model resolution on these mechanisms. Moreover, ARPEGE tends

to enhance the role of the VMM and PAM in shaping the divergence/convergence field.

The benefits of increased model resolution on the representation of mean precipitation over the GS were shown in Minobe et al. (2008). They showed that sharper SST gradients can lead to narrower and more intense precipitation over the GS, and a better consistency with satellite observations. Our analysis indicates that this feature is mainly visible near the coast for the lowest decile of ASII and offshore over the convergence zone for the highest deciles of ASII.

Our results highlight the role the atmospheric circulation and associated anomalous winds in the location, strength, and occurrence of VMM and PAM. They also reveal the suitability of performing clustering approaches to isolate different atmospheric circulation regimes to better understand the MABL mechanisms and their role in modulating the atmospheric response to SST front and associated mesoscale variability.

Acknowledgments. The financial support for this study has been provided by the French Ministry through a Ph.D. fellowship. This work is a contribution to the H2020-PRIMAVERA project (Process-Based Climate Simulation: Advances in High-Resolution Modelling and European Climate Risk Assessment) and to the HighResMIP/WRCP international initiative. The authors give special thanks to Arnaud Czaja, Hervé Giordani, Justin Small, and Rhys Parfitt for their interesting and constructive discussions. The authors also thank the three anonymous reviewers for their careful reading, the interest they gave to our study, and their insightful comments, which helped us to improve the paper.

Data availability statement. Datasets for each one of the variables used in this article are available at the Earth System Grid Federation (ESGF; Kennedy et al. 2017) for the full 10 members for both the high-resolution (HR) and low-resolution (LR) versions of the model. The ERA5 and ERA-Interim reanalysis datasets are available at the ECMWF website (https://www.ecmwf.int/en/forecasts/datasets/browse-reanalysis-datasets).

REFERENCES

Bellucci, A., and Coauthors, 2021: Air–sea interaction over the Gulf Stream in an ensemble of HighResMIP present climate simulations. *Climate Dyn.*, **56**, 2093–2111, https://doi.org/10.1007/s00382-020-05573-z.

Berrisford, P., D. Dee, K. Fielding, M. Fuentes, P. Kallberg, S. Kobayashi, and S. Uppala, 2009: The ERA-Interim Archive. ERA Rep. Series 1, 16 pp., https://www.ecmwf.int/node/8173.

Brachet, S., F. Codron, Y. Feliks, M. Ghil, H. Le Treut, and E. Simonnet, 2012: Atmospheric circulations induced by a midlatitude SST front: A GCM study. *J. Climate*, **25**, 1847–1853, https://doi.org/10.1175/JCLI-D-11-00329.1.

Bryan, F. O., R. Tomas, J. M. Dennis, D. B. Chelton, N. G. Loeb, and J. L. McClean, 2010: Frontal scale air–sea interaction in high-resolution coupled climate models. *J. Climate*, **23**, 6277–6291, https://doi.org/10.1175/2010JCLI3665.1.

Chang, E. K., S. Lee, and K. L. Swanson, 2002: Storm track dynamics. *J. Climate*, **15**, 2163–2183, https://doi.org/10.1175/1520-0442(2002)015<02163:STD>2.0.CO;2.

Chelton, D. B., and S.-P. Xie, 2010: Coupled ocean–atmosphere interaction at oceanic mesoscales. *Oceanography*, **23**, 52–69, https://doi.org/10.5670/oceanog.2010.05.

——, and Coauthors, 2001: Observations of coupling between surface wind stress and sea surface temperature in the eastern tropical Pacific. *J. Climate*, **14**, 1479–1498, https://doi.org/10.1175/1520-0442(2001)014<1479:OOCBSW>2.0.CO;2.

——, M. G. Schlax, M. H. Freilich, and R. F. Milliff, 2004: Satellite measurements reveal persistent small-scale features in ocean winds. *Science*, **303**, 978–983, https://doi.org/10.1126/science.1091901.

Eyring, V., S. Bony, G. A. Meehl, C. A. Senior, B. Stevens, R. J. Stouffer, and K. E. Taylor, 2016: Overview of the Coupled Model Intercomparison Project phase 6 (CMIP6) experimental design and organization. *Geosci. Model Dev.*, **9**, 1937–1958, https://doi.org/10.5194/gmd-9-1937-2016.

Haarsma, R. J., and Coauthors, 2016: High Resolution Model Intercomparison Project (HighResMIP v1.0) for CMIP6. *Geosci. Model Dev.*, **9**, 4185–4208, https://doi.org/10.5194/gmd-9-4185-2016.

Hayes, S., M. McPhaden, and J. Wallace, 1989: The influence of sea-surface temperature on surface wind in the eastern equatorial Pacific: Weekly to monthly variability. *J. Climate*, **2**, 1500–1506, https://doi.org/10.1175/1520-0442(1989)002<1500:TIOSST>2.0.CO;2.

Hersbach, H., 2018: Operational global reanalysis: Progress, future directions and synergies with NWP. ERA Rep. Series 27, 63 pp., https://www.ecmwf.int/node/18765.

——, and Coauthors, 2020: The ERA5 global reanalysis. *Quart. J. Roy. Meteor. Soc.*, **146**, 1999–2049, https://doi.org/10.1002/qj.3803.

Kennedy, J., H. Titchner, N. Rayner, and M. Roberts, 2017: input4MIPs.MOHC.SSTsAndSeaIce.HighResMIP.MOHC-HadISST-2-2-0-0-0. Version 5 May 2017, Earth System Grid Federation, accessed October 2017, https://doi.org/10.22033/ESGF/input4MIPs.1221.

Kuwano-Yoshida, A., S. Minobe, and S.-P. Xie, 2010: Precipitation response to the Gulf Stream in an atmospheric GCM. *J. Climate*, **23**, 3676–3698, https://doi.org/10.1175/2010JCLI3261.1.

Lindzen, R. S., and S. Nigam, 1987: On the role of sea surface temperature gradients in forcing low-level winds and convergence in the tropics. *J. Atmos. Sci.*, **44**, 2418–2436, https://doi.org/10.1175/1520-0469(1987)044<2418:OTROSS>2.0.CO;2.

Ma, X., and Coauthors, 2016: Western boundary currents regulated by interaction between ocean eddies and the atmosphere. *Nature*, **535**, 533–537, https://doi.org/10.1038/nature18640.

Masunaga, R., H. Nakamura, B. Taguchi, and T. Miyasaka, 2020a: Processes shaping the frontal-scale time-mean surface wind convergence patterns around the Gulf Stream and Agulhas Return Current in winter. *J. Climate*, **33**, 9083–9101, https://doi.org/10.1175/JCLI-D-19-0948.1.

——, ——, ——, and ——, 2020b: Processes shaping the frontal-scale time-mean surface wind convergence patterns around the Kuroshio Extension in winter. *J. Climate*, **33**, 3–25, https://doi.org/10.1175/JCLI-D-19-0097.1.

Minobe, S., A. Kuwano-Yoshida, N. Komori, S.-P. Xie, and R. J. Small, 2008: Influence of the Gulf Stream on the troposphere. *Nature*, **452**, 206–209, https://doi.org/10.1038/nature06690.

——, M. Miyashita, A. Kuwano-Yoshida, H. Tokinaga, and S.-P. Xie, 2010: Atmospheric response to the Gulf Stream: Seasonal variations. *J. Climate*, **23**, 3699–3719, https://doi.org/10.1175/2010JCLI3359.1.

Ogawa, F., and T. Spengler, 2019: Prevailing surface wind direction during air–sea heat exchange. *J. Climate*, **32**, 5601–5617, https://doi.org/10.1175/JCLI-D-18-0752.1.

O'Neill, L. W., D. B. Chelton, and S. K. Esbensen, 2003: Observations of SST-induced perturbations of the wind stress field over the Southern Ocean on seasonal timescales. *J. Climate*, **16**, 2340–2354, https://doi.org/10.1175/2780.1.

——, ——, and ——, 2010: The effects of SST-induced surface wind speed and direction gradients on midlatitude surface vorticity and divergence. *J. Climate*, **23**, 255–281, https://doi.org/10.1175/2009JCLI2613.1.

——, T. Haack, D. B. Chelton, and E. Skyllingstad, 2017: The Gulf Stream convergence zone in the time-mean winds. *J. Atmos. Sci.*, **74**, 2383–2412, https://doi.org/10.1175/JAS-D-16-0213.1.

Parfitt, R., 2014: Extreme air–sea interactions over the Gulf Stream. Ph.D. thesis, Imperial College London, 189 pp., https://core.ac.uk/download/pdf/76994906.pdf.

——, and A. Czaja, 2016: On the contribution of synoptic transients to the mean atmospheric state in the Gulf Stream region. *Quart. J. Roy. Meteor. Soc.*, **142**, 1554–1561, https://doi.org/10.1002/qj.2689.

——, and H. Seo, 2018: A new framework for near-surface wind convergence over the Kuroshio Extension and Gulf Stream in wintertime: The role of atmospheric fronts. *Geophys. Res. Lett.*, **45**, 9909–9918, https://doi.org/10.1029/2018GL080135.

——, A. Czaja, S. Minobe, and A. Kuwano-Yoshida, 2016: The atmospheric frontal response to SST perturbations in the Gulf Stream region. *Geophys. Res. Lett.*, **43**, 2299–2306, https://doi.org/10.1002/2016GL067723.

Piazza, M., L. Terray, J. Boé, E. Maisonnave, and E. Sanchez-Gomez, 2016: Influence of small-scale North Atlantic sea surface temperature patterns on the marine boundary layer and free troposphere: A study using the atmospheric ARPEGE model. *Climate Dyn.*, **46**, 1699–1717, https://doi.org/10.1007/s00382-015-2669-z.

Putrasahan, D. A., A. J. Miller, and H. Seo, 2013: Isolating mesoscale coupled ocean–atmosphere interactions in the Kuroshio Extension region. *Dyn. Atmos. Oceans*, **63**, 60–78, https://doi.org/10.1016/j.dynatmoce.2013.04.001.

Roberts, M. J., H. T. Hewitt, P. Hyder, D. Ferreira, S. A. Josey, M. Mizielinski, and A. Shelly, 2016: Impact of ocean resolution on coupled air–sea fluxes and large-scale climate. *Geophys. Res. Lett.*, **43**, 10 430–10 438, https://doi.org/10.1002/2016GL070559.

——, and Coauthors, 2020: Impact of model resolution on tropical cyclone simulation using the HighResMIP–PRIMAVERA multimodel ensemble. *J. Climate*, **33**, 2557–2583, https://doi.org/10.1175/JCLI-D-19-0639.1.

Roehrig, R., and Coauthors, 2020: The CNRM global atmosphere model ARPEGE-Climat 6.3: Description and evaluation. *J. Adv. Model. Earth Syst.*, **12**, e2020MS002075, https://doi.org/10.1029/2020MS002075.

Rowell, D. P., 2019: An observational constraint on CMIP5 projections of the East African long rains and southern Indian Ocean warming. *Geophys. Res. Lett.*, **46**, 6050–6058, https://doi.org/10.1029/2019GL082847.

Shimada, T., and S. Minobe, 2011: Global analysis of the pressure adjustment mechanism over sea surface temperature fronts using AIRS/Aqua data. *Geophys. Res. Lett.*, **38**, L06704, https://doi.org/10.1029/2010GL046625.

Simmons, A., S. Uppala, D. Dee, and S. Kobayashi, 2007: ERA-Interim: New ECMWF reanalysis products from 1989 onwards. *ECMWF Newsletter*, No. 110, ECMWF, Reading, United Kingdom, 25–35, https://www.ecmwf.int/node/17713.

Small, R. J., and Coauthors, 2008: Air–sea interaction over ocean fronts and eddies. *Dyn. Atmos. Oceans*, **45**, 274–319, https://doi.org/10.1016/j.dynatmoce.2008.01.001.

Spall, M. A., 2007: Midlatitude wind stress–sea surface temperature coupling in the vicinity of oceanic fronts. *J. Climate*, **20**, 3785–3801, https://doi.org/10.1175/JCLI4234.1.

Sweet, W., R. Fett, J. Kerling, and P. La Violette, 1981: Air–sea interaction effects in the lower troposphere across the north wall of the Gulf Stream. *Mon. Wea. Rev.*, **109**, 1042–1052, https://doi.org/10.1175/1520-0493(1981)109<1042:ASIEIT>2.0.CO;2.

Takatama, K., S. Minobe, M. Inatsu, and R. J. Small, 2015: Diagnostics for near-surface wind response to the Gulf Stream in a regional atmospheric model. *J. Climate*, **28**, 238–255, https://doi.org/10.1175/JCLI-D-13-00668.1.

Thomas, M., A. Devasthale, T. L'Ecuyer, S. Wang, T. Koenigk, and K. Wyser, 2019: Snowfall distribution and its response to the Arctic Oscillation: An evaluation of HighResMIP models in the Arctic using CPR/CloudSat observations. *Geosci. Model Dev.*, **12**, 3759–3772, https://doi.org/10.5194/gmd-12-3759-2019.

Tokinaga, H., Y. Tanimoto, S.-P. Xie, T. Sampe, H. Tomita, and H. Ichikawa, 2009: Ocean frontal effects on the vertical development of clouds over the western North Pacific: In situ and satellite observations. *J. Climate*, **22**, 4241–4260, https://doi.org/10.1175/2009JCLI2763.1.

Vannière, B., A. Czaja, H. Dacre, and T. Woollings, 2017: A "cold path" for the Gulf Stream–troposphere connection. *J. Climate*, **30**, 1363–1379, https://doi.org/10.1175/JCLI-D-15-0749.1.

Voldoire, A., and Coauthors, 2019: Evaluation of CMIP6 deck experiments with CNRM-CM6-1. *J. Adv. Model. Earth Syst.*, **11**, 2177–2213, https://doi.org/10.1029/2019MS001683.

Wallace, J. M., T. Mitchell, and C. Deser, 1989: The influence of sea-surface temperature on surface wind in the eastern equatorial Pacific: Seasonal and interannual variability. *J. Climate*, **2**, 1492–1499, https://doi.org/10.1175/1520-0442(1989)002<1492:TIOSST>2.0.CO;2.

Xie, S.-P., J. Hafner, Y. Tanimoto, W. T. Liu, H. Tokinaga, and H. Xu, 2002: Bathymetric effect on the winter sea surface temperature and climate of the Yellow and East China Seas. *Geophys. Res. Lett.*, **29**, 2228, https://doi.org/10.1029/2002GL015884.

Yessad, K., 2015: Basics about ARPEGE/IFS, ALADIN and AROME in the cycle 46t1r1 of ARPEGE/IFS, UMR-CNRM, accessed August 2020, https://www.umr-cnrm.fr/gmapdoc/spip.php?article29.